applied sciences

MDPI

Article

Investigation on Numerical Simulation of VIV of Deep-Sea Flexible Risers

Liyuan Jia [1], Song Sang [1,*], Xiao Shi [2] and Fukui Shen [1]

[1] School of Engineering, Ocean University of China, Qingdao 266404, China; jialiyuan77@163.com (L.J.); shenfukui2023@163.com (F.S.)
[2] School of Intelligent Manufacturing, Qingdao Huanghai University, Qingdao 266427, China; shixiao2206@163.com
* Correspondence: sangqi@ouc.edu.cn; Tel.: +86-135-7383-0323

Abstract: The vortex-induced vibration (VIV) of flexible risers is a complex fluid–structure interaction (FSI) phenomenon. In this study, we conducted a numerical simulation method based on the slicing method to study the vortex-induced vibration (VIV) of deep-sea flexible risers with different slenderness ratios and uniform flow velocities. The method combines the finite element model of the riser structure with the two-dimensional flow field slices solved by the Fluent solver. The fluid–structure interaction was realized by a self-compiled UDF program and the overset mesh technique. The numerical results were validated by comparing them with experimental data. The VIV characteristics of the riser, such as the vibration track, vibration mode, vibration frequency and wake vortex shedding mode, were analyzed. The article reveals the nonlinear dynamic features of flexible riser vibration, such as multi-frequency vibration, wide-frequency vibration and multi-modal vibration. The article also provides insights into the fluid–structure interaction mechanism of VIV of deep-sea flexible risers.

Keywords: flexible riser; vortex-induced vibration; mufti-strip method; mufti-modal vibration

check for updates

Citation: Jia, L.; Sang, S.; Shi, X.; Shen, F. Investigation on Numerical Simulation of VIV of Deep-Sea Flexible Risers. *Appl. Sci.* **2023**, *13*, 8096. https://doi.org/10.3390/app13148096

Academic Editors: Baiqiao Chen, He Li, Yichao Liu and Chenggeng Huang

Received: 12 June 2023
Revised: 5 July 2023
Accepted: 6 July 2023
Published: 11 July 2023

Copyright: © 2023 by the authors. Licensee MDPI, Basel, Switzerland. This article is an open access article distributed under the terms and conditions of the Creative Commons Attribution (CC BY) license (https://creativecommons.org/licenses/by/4.0/).

1. Introduction

Vortex-induced vibration (VIV) occurs due to the alternating shedding vortex formed by the instantaneous variable pressure difference on both sides of a structure. However, VIV increases the dynamic load of the structure [1] and can cause fatigue failure when subjected to long-term action. If deep-sea oil and gas pipelines suffer from fatigue damage and fracture, large amounts of oil and gas can leak into the ocean, causing serious environmental pollution and ecological disasters. Therefore, studying the dynamic response of VIV in deep-sea flexible risers is of great significance to accurately predict their fatigue damage.

As early as 1981, Vandiver et al. [2], a group of researchers in the United States, carried out VIV experiments of slender flexible risers using rising and falling tides. In 1997, Lie H et al. [3] carried out a VIV experiment of risers under shear flow on the west coast of Norway. In 2008, Tognarelli et al. [4] monitored the VIV characteristics of risers in the Gulf of Mexico within the water depth range of 360 m~2070 m.

However, large-scale outdoor riser VIV experiments still have some shortcomings in the control of specific experimental parameters and data measurements. Therefore, researchers have begun to conduct indoor experimental research on the VIV of flexible risers in large water tanks.

Professor Chaplin and Professor Bearman [5] led a group of researchers to carry out a drag experiment focused on the VIV of a slender riser in a large water tank. The experimental results of the riser VIV response were compared with the predictions obtained by 11 different numerical methods (six CFD models and five empirical models), and it was found that the crossflow (CF) displacement predicted by the empirical models was more successful than that predicted by the CFD models. Wilde [6] conducted an experimental

study on the VIV of a flexible riser in a towing tank. The flow field profile demonstrated uniform flow, and the three-dimensional vibration response characteristics of the flexible riser were successfully captured. A VIV test of a flexible riser with a slenderness ratio of 481.5 was carried out by Tognarelli [7]. It was shown that (a) with an increase in flow velocity, the maximum displacement of the vortex-induced vibration of the riser increased; (b) the vibration frequency of the riser in the IL direction was twice that in the CF direction; and (c) the vibration modes excited in the CF direction reached up to the eighth order, while those excited in the IL direction reached up to the twelfth order.

Since the length of a deep-sea flexible riser can reach 400~1500 m and operation in outdoor and laboratory tank tests is difficult, research on the VIV of deep-sea flexible risers using the numerical analysis method has attracted the attention of researchers. Numerical analysis methods for slender flexible risers are mainly divided into two categories: one is based on experimental data, such as empirical and semi-empirical models, and the other is the numerical simulation method based on computational fluid dynamics (CFD) and computational structural dynamics (CSD) [8].

Empirical and semi-empirical models need to be supported by massive experimental experiences, where the ranges of key parameters are given by fitting the experimental results. As early as 1964, Bishop and Hassan [9] proposed the Van der Pol wake oscillator model. B. Afra, A. Amiri Delouei and A. Tarokh proposed a hybrid model that included an explicit Lattice Spring Model and an Immersed Boundary–non-Newtonian Lattice Boltzmann Method to simulate the behavior of filament in the vicinity of fluid flow. They also studied the effects of the fluid and structural characteristics on the motion of the filament and cylinder [10]. After more than half a century, an increasing number of empirical models have been proposed by scholars [11–15]. However, mode transition is an important feature of the VIV response of long flexible risers, but the empirical model cannot account for this switching process.

The numerical simulation method has become an indispensable complement to experiments in ocean engineering [16]. With improvement in computing efficiency, the VIV study of long flexible risers using numerical models has become increasingly common. However, with the increase in the riser slenderness ratio, three-dimensional numerical simulation has become increasingly difficult. Therefore, numerical simulation of risers' VIV coupled with a two-dimensional fluid and three-dimensional structure based on the slice method has attracted the attention of researchers.

In 2004, Menegini J.R. [17] adopted the discrete vortex method (DVM) to establish a quasi-three-dimensional riser vortex-induced vibration model and solved the structural part of the dynamic equation according to the Euler–Bernoulli beam theory. The numerical simulation results of flexible riser VIV at different flow velocities were compared with the experimental results, and it was observed that the wake vortex shedding mode was 2P for the riser with a larger amplitude and 2S for the riser with a smaller amplitude. B. Afra and S. Karimnejad [18] used the Lattice Spring Method (LSM) combined with the Immersed Boundary–Lattice Boltzmann Method (IB–LBM) to investigate fluid–elastic body interaction problems in unsteady conditions. The LSM needs no arbitrary spring parameters to determine the deformation of the flexible body. Schulz and Meling [19] combined the RANS method and finite element method to solve the structural dynamic response, divided the response into multiple slices to establish a quasi-three-dimensional model, and carried out VIV numerical simulation research on a flexible riser under shear flow. The researchers used this method to analyze the VIV response of the top tension riser.

WAN D.C. et al. [20–23] developed a computational fluid dynamics (CFD) solver, VIV FOAM SJTU, on the Open FOAM platform based on the slice method, and amplitudes of the risers in the IL and CF directions were accurately predicted. In 2020, Han [24], based on the Fluent solver and a self-compiled UDF, carried out numerical simulation research on a three-dimensional flexible riser vortex-induced vibration under different flow speeds and demonstrated the phenomenon of the adjacent order vibration mode switching of the flexible riser vortex-induced vibration with a change in flow velocity. The phenomena

of the "traveling wave" and "standing wave" of the flexible riser were observed. At the same time, the frequency of the VIV response of a flexible riser was analyzed, and the phenomenon of multi-frequency vibration was observed. In particular, it was found that the vortex-induced vibration characteristics of the riser showed a vibration response with a wide-band spectrum when the inflow velocity was relatively high.

In this paper, we accurately predict the fatigue damage of deep-sea flexible risers, and numerical analysis methods based on the slicing method offer valuable insights into the dynamic response of vortex-induced vibration. Using a self-compiled UDF program and overset mesh technique to reveal the nonlinear dynamic features of flexible riser vibration, our research focuses on further improving these numerical simulation methods to provide more accurate and reliable predictions of fatigue damage in deep-sea flexible risers.

2. Numerical Simulation Method of VIV of Riser

2.1. Fluid-Domain Governing Equations

Viscous fluid flow is the macroscopic incompressible motion of fluid that abides by the laws of mass conservation, momentum conservation and energy conservation and is subject to the governing equations of the fluid. In this paper, we did not consider the energy conversion caused by temperature change during simulation; hence, we did not use the energy equation. Viscous fluid flow satisfies the Navier–Stokes (N–S) equation, and we employed the Reynolds-averaged numerical simulation (RANS) method. In this method, the Reynolds-averaged N–S equation is used to describe the fluid flow instead of the N–S equation. In Cartesian coordinates:

Continuity equation:

$$\frac{\partial \overline{u_i}}{\partial x_i} = 0 \tag{1}$$

Momentum equation:

$$\rho \frac{\partial \overline{u_i}}{\partial t} + \rho \frac{\partial \overline{u_i u_j}}{\partial x_j} = -\frac{\partial \overline{p}}{\partial x_i} + \mu \nabla^2 \overline{u_i} - \rho \frac{\partial \overline{u'_i u'_j}}{\partial x_j} \tag{2}$$

where i and j take values of 1, 2 or 3, which, respectively, represent the components of variables in the X, Y and Z directions; P denotes the pressure; ∇ is the Hamiltonian operator; $\overline{u}_i$ and $\overline{u}_j$ stand for the time-average flow rate; and $\overline{u'}_i$ and $\overline{u'}_j$ signify the time-average value of the pulsating flow rate.

Compared with the N–S equation, the RANS equation adds a group of unknown Reynolds stress terms which makes the RANS equation an unclosed equation. To solve the RANS equation, we must add a new supplementary equation known as the turbulence model.

The boundary layer gradient around a flow is large, and an obvious pressure gradient and shearing action exist. Therefore, in this paper, we use the shearing pressure transmission turbulence model. This model was proposed by Menter [25] in 1993 and can better capture the flow around and wake vortex near the wall. The model includes two equations: one for turbulent kinetic energy k and one for dissipation rate ω.

$$\rho \frac{\partial k}{\partial t} + k\rho \frac{\partial u_i}{\partial x_i} = \frac{\partial}{\partial x_j}\left(\Gamma_k \frac{\partial k}{\partial x_j}\right) + \widetilde{G}_k - Y_k + S_k \tag{3}$$

$$\rho \frac{\partial \omega}{\partial t} + \rho\omega \frac{\partial u_i}{\partial x_i} = \frac{\partial}{\partial x_j}\left(\Gamma_\omega \frac{\partial \omega}{\partial x_j}\right) + G_\omega - Y_\omega + D_\omega + S_\omega \tag{4}$$

where $\widetilde{G}_k$ denotes the turbulence kinetic energy produced by the average velocity gradient, G_ω signifies the turbulent kinetic energy generated by the equation, Γ_k and Γ_ω represent the effective diffusivities of k and ω, Y_k and Y_ω stand for turbulence terms due to diffusion, D_ω is the orthogonal divergence term, and S_k and S_ω are the source phases of the equation.

To solve the governing equation of the fluid, we used the finite volume method in discrete form. We used the Fluent solver, which employs the coupled algorithm and overlapping grid technology. The second-order upwind scheme was used for the transient equation, and the fully implicit scheme was used for time dispersion.

2.2. Structural Dynamic Model of Riser

The top tension flexible riser model was simplified as a Euler–Bernoulli beam, with the same material and section shape assumed along the riser's length. We took the in-line (IL) direction as the X axis, the crossflow (CF) direction as the Y axis and the riser length direction as the Z axis, as shown in Figure 1. The differential equations of structural motion in the flow direction are given by [26,27]:

$$\frac{\partial^2}{\partial z^2}\left[EI\frac{\partial^2 u_i(z,t)}{\partial z^2}\right] - \frac{\partial}{\partial z}\left[T(z)\frac{\partial u_i(z,t)}{\partial z}\right] + m\frac{\partial^2 u_i(z,t)}{\partial t^2} + c\frac{\partial u_i(z,t)}{\partial t} = F_i(z,t) \quad (5)$$

where EI is the bending stiffness, EA is the tensile stiffness, m is the riser mass per unit length and c is the structural damping. $u_i(z,t)$ denotes the CF and IL displacement, and $F_i(z,t)$ denotes the CF direction and the IL hydrodynamic force (in which i = 1 is the IL direction, and i = 2 is the CF direction). $T(z)$ is the riser top tension.

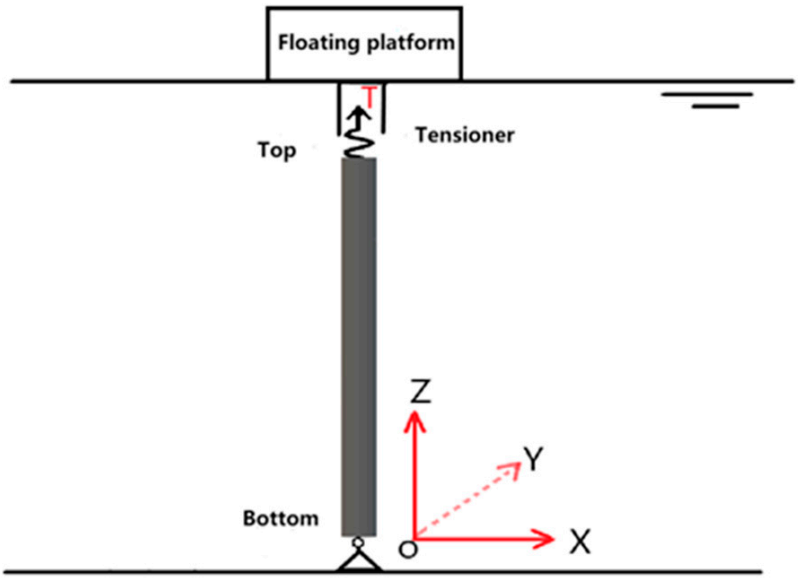

Figure 1. Riser model diagram.

Willden and Graham [28] studied the transverse vibration responses of a rigid cylinder. Their model allowed for three degrees of freedom, including axial and transverse displacements and a rotation about an axis perpendicular to the plane of the displacements. Yamamoto [29] also used the same three degrees of freedom per finite element node to investigate hydro-elastic interactions between oscillating flexible cylinders and fluid forces. However, this simplified finite element method can only reflect the riser's response in the transverse direction.

To study the dynamic responses of deep-sea risers in both the transverse and downstream directions, we reduced the riser to a sufficient number of three-dimensional finite elements, each of which had six degrees of freedom. The finite element diagram is shown in Figure 2.

The load vector of each element can be expressed as:

$$F^e = [F_{1x}, F_{1y}, F_{1z}, F_{1\theta_x}, F_{1\theta_y}, F_{1\theta_z}, F_{2x}, F_{2y}, F_{2z}, F_{2\theta_x}, F_{2\theta_y}, F_{2\theta_z}]^{\mathrm{T}} \quad (6)$$

The positions of some nodes were taken as the positions of the two-dimensional flow field slices, and the fluid acting force at the slice node was simplified as the uniformly distributed load plus the riser unit near the slice. The positional relationship between the slices and the finite element and the force exerted on the element are shown in Figure 3.

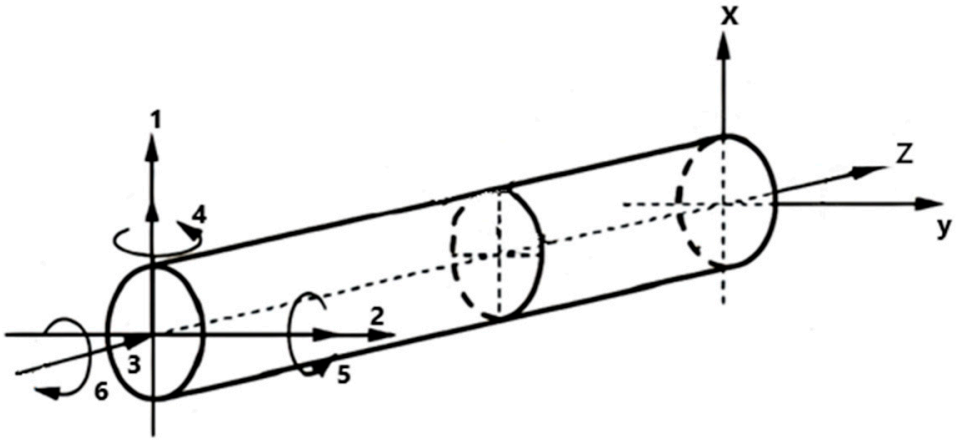

Figure 2. Finite element diagram of the riser.

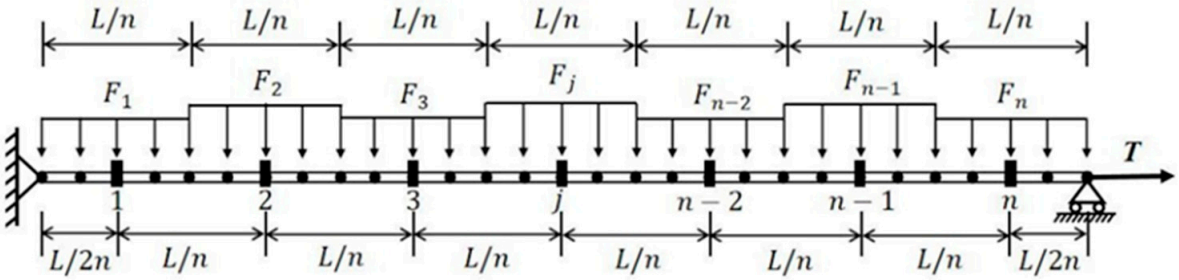

Figure 3. Riser slice division and finite element layout.

By discretizing Equation (5) using the finite element method, we obtained the following equation [26,27]:

$$[M]\{\ddot{x}_i(t)\} + [C]\{\dot{x}_i(t)\} + ([K_E] + [K_G])\{x_i(t)\} = \{F_i(t)\} \tag{7}$$

where $[M]$, $[C]$, $[K_E]$ and $[K_G]$ denote the global matrices of the mass, the damping, the elastic stiffness of the riser and geometric stiffness; $\ddot{x}_i(t)$, $\dot{x}_i(t)$ and $x_i(t)$ represent the vectors of the accelerations, velocities and deflections of the nodes of the riser, respectively; and $\{F_i(t)\}$ signifies the load vector in the x–y direction. The Newmark-β method was used to solve the motion equation.

The structural damping usually depends on the natural frequency. In actual analysis, we usually adopt the Rayleigh damping matrix, which is a linear combination of $[M]$ and $[K]$ [30]:

$$[C] = \alpha[M] + \gamma[K] \tag{8}$$

where α and γ are the Rayleigh damping coefficient, which is related to the natural frequency and damping ratio of the riser [30]:

$$\begin{bmatrix} \alpha \\ \gamma \end{bmatrix} = \frac{2\zeta}{\omega_n + \omega_m} \begin{bmatrix} \omega_n \omega_m \\ 1 \end{bmatrix} \tag{9}$$

where $\zeta = 0.03$, ω_n takes the first-order natural frequency and ω_m takes the natural frequency with a relatively high contribution to the vibration response.

2.3. Overset Mesh Technique

Traditional moving mesh technology has the drawback that even slight movement in one part can affect the overall situation, which consumes significant computing time and requires high grid quality. Moreover, when the grid is moving fast or has large deformations, it is prone to distortion, leading to negative volume during dynamic updates.

To address these issues, Fluent has introduced a new mesh function called the overset mesh technique. With this technique, the entire computational domain is divided into a background area and a foreground area corresponding to the moving parts. Mesh division is performed separately for each area, and an overset interface is created to link the foreground and background meshes. Data transfer between the two regions is achieved through interpolation.

Tezdogan et al. [31] used the overset mesh technology to build a full-scale KRISO container ship model for nonlinear unsteady RANS simulation. The authors found that important flow characteristics, such as flow separation, slamming, wave breaking and high vortices around the hull, remained within the overset domain.

2.4. Method of Fluid–Structure Interaction (FSI)

Fluid–structure interaction (FSI) occurs due to the coupling between a fluid and a solid structure. The solid structure experiences motion response or deformation under the action of flow field force, while the deformation or motion reaction of the solid structure affects the fluid, causing a change in fluid force at the next moment.

The vortex-induced vibration (VIV) problem is a classical FSI problem that requires a comprehensive consideration of the interaction between flow field motion parameters and structural motion parameters during analysis. On one hand, the cylinder in the flow field experiences fluid force, causing parameters such as amplitude, velocity and acceleration to change. On the other hand, the cylinder parameters affect the flow field, leading to changes in the flow field motion parameters.

For quasi-3D FSI solutions based on the slice method, we followed these steps, as shown in Figure 4:

1. At the initial moment, the riser structure was fixed, and the flow field was calculated. Each flow field slice simultaneously solved the governing equation of the fluid to obtain the fluid force of each slice node;
2. The self-compiled UDF [32] program cylinder.c called the Computer_Force_And_Moment macro to extract the fluid force on the slice node at the current moment and to simplify the fluid force into uniformly distributed loads acting on the finite elements represented by each slice;
3. Uniformly distributed loads acting on the elements were converted into node loads by an equivalent load method. We solved the dynamic equation of the riser structure using the Newmark-β method to obtain the displacement, velocity and acceleration of the finite element nodes at the current moment;
4. The cylinder.c program called the DEFINE_CG_MOTION macro to transmit the displacement and speed of finite element nodes at the slice calculated in the previous step back to Fluent to update the displacement and speed of the cylinder in the slice. We then realized the mesh update in the fluid domain by combining the overset mesh technology;
5. We entered the next time step and repeated until the set total time was reached and the calculation was completed.

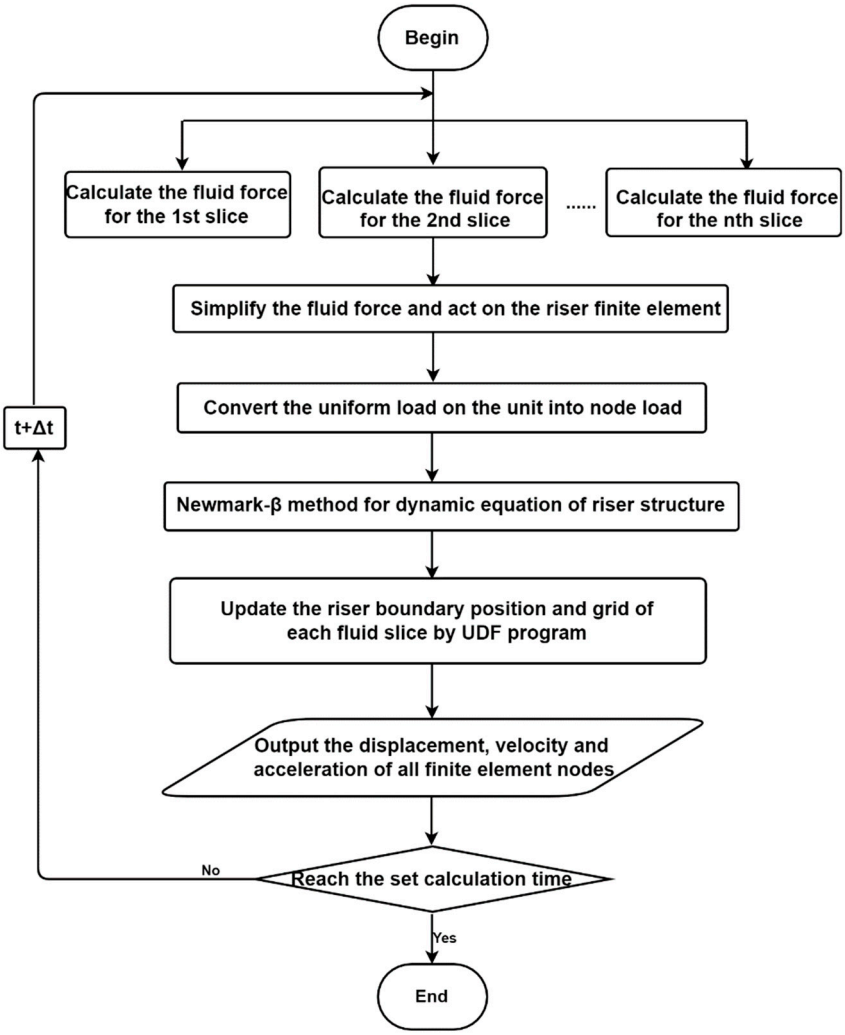

Figure 4. Flow chart of fluid–structure interaction based on the slice method.

3. Quasi-3D Numerical Calculation Model

3.1. Computational Domain and Boundary Conditions

The computational domain for the flow field calculation was set as 30D × 60D, with distances from the inlet boundary and upper and lower boundaries to the riser center at 15D [33,34]. The distance from the outlet boundary to the riser center was 45D, as shown in Figure 5.

The corresponding boundary settings are given in Table 1.

3.2. Grid Division

Matching the overset mesh technique, the grid division consisted of a background mesh and a foreground grid, and an overset interface was adopted at the junction of the two grids. The background grid was generated in the entire computational domain to ensure that interpolation points could be found in the background grid for any moving region at any moment.

It is important to note that the overset area requires a fine enough grid; otherwise, a floating-point overflow may occur, leading to interpolation failure. In the background grid, the 5D × 5D area centered on the riser was encrypted, as shown in Figure 6. For the foreground grid, there was no fluid information, and the boundary layer region adjacent to the cylinder wall moved synchronously with the cylinder. A dot representing the center of the riser was used as a reference, with a foreground grid area of radius 1.5D.

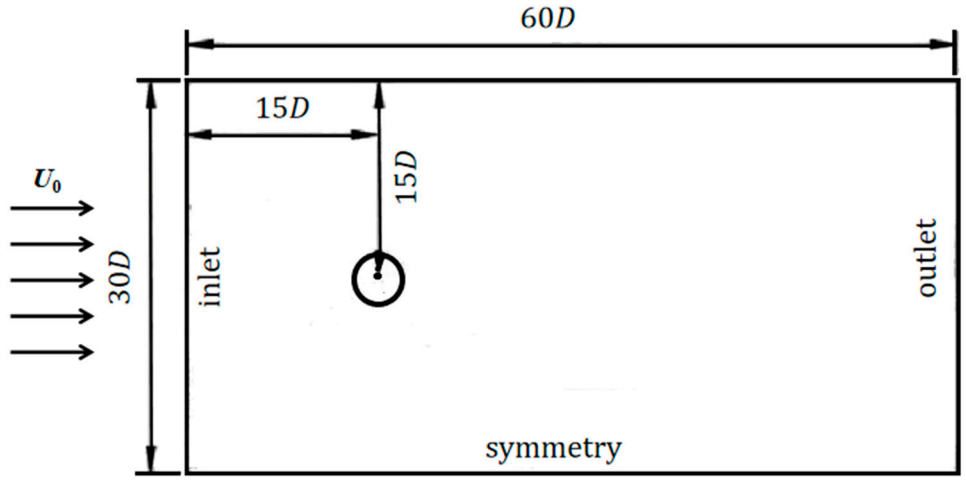

Figure 5. Computational domain.

Table 1. Boundary settings.

Boundary	Setting
Inlet boundary	Velocity-inlet, $u = U_0$, $v = 0$
Outlet boundary	Pressure-outlet, $\partial u/\partial x = 0$, $\partial v/\partial x = 0$, static pressure = 0
Upper and lower boundary	Symmetry, $\partial u/\partial x = 0$, $\partial v/\partial x = 0$
Cylinder boundary	No-Slip Wall, $u = v = 0$
Interface of foreground grid and background grid	Overset Interface

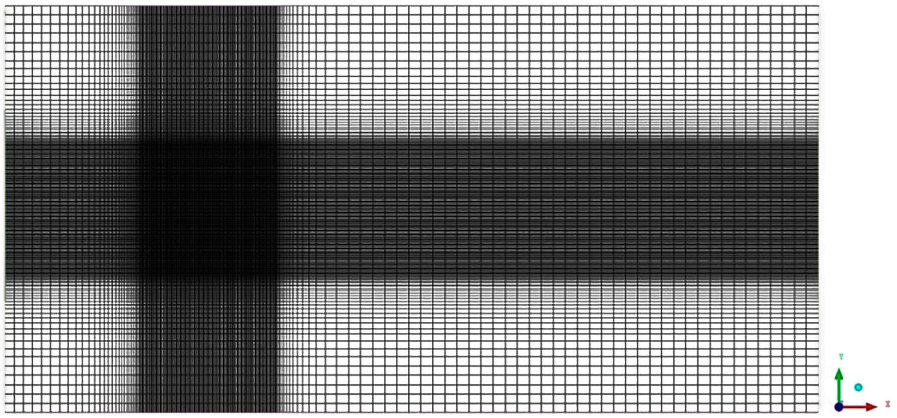

Figure 6. Background grid diagram.

An O-type mesh generation was used for mesh refinement, where the mesh near the wall of the cylinder met y+<1, as shown in Figure 7. Finally, the overset mesh technique was used to realize the coupling link between the foreground grid and the background grid, forming a single two-dimensional flow field grid, as shown in Figure 8.

3.3. Quasi-3D Numerical Model Validation

To verify the accuracy of the quasi-3D numerical model, we selected a working condition from a top tension riser experiment [35] conducted by the Norwegian Institute of Marine Technology. Table 2 shows the properties of the riser model.

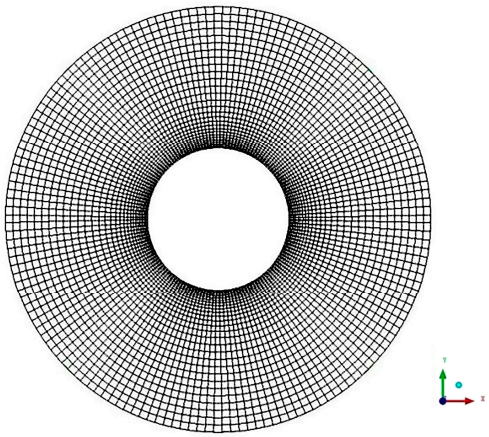

Figure 7. Foreground grid diagram.

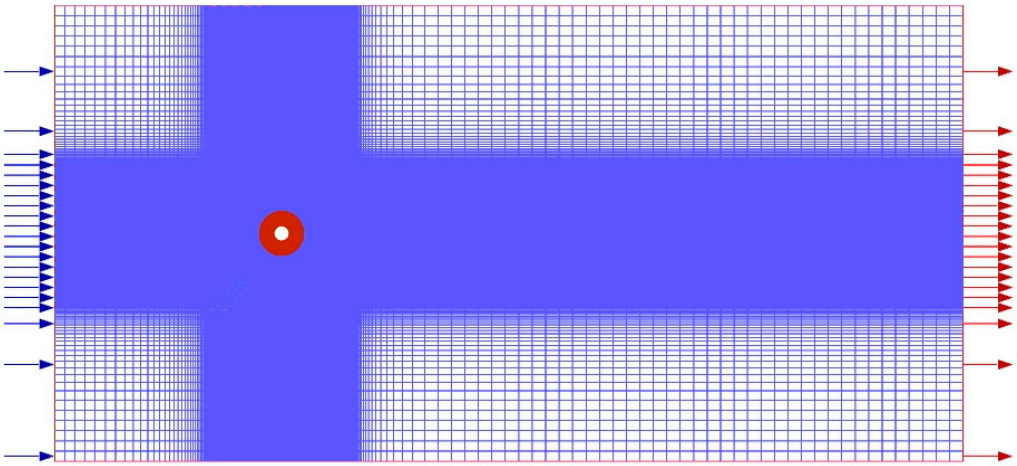

Figure 8. Grid division diagram of single 2D flow field slice.

Table 2. Properties of the riser model.

Properties	Values	Units
Riser outer diameter (D)	0.02	m
Riser wall thickness (tw)	0.0045	m
Length of the riser (L)	9.63	m
Top tension (T)	817	N
Young's modulus (E)	1.025 × 1011	N/m^2
Mass ratio (m *)	2.23	
First-order eigenfrequency (f1)	1.79	Hz
Second-order eigenfrequency (f2)	3.67	Hz

*: Dimensionless.

To accurately simulate the vibration pattern of the riser, it was ensured that at least three slices and seven finite element nodes were available for each mode. The axial direction of the riser was uniformly divided into 1–69 finite element nodes from bottom to top, with 17 two-dimensional flow field slices arranged. The 9th slice was located at the 35th finite element node, which was in the center of the riser. Figure 9 shows the schematic diagram of slice division.

Numerical simulation of the vortex-induced vibration of a riser was performed. Figure 10 shows the comparison of the envelopes of the inline displacement between the present quasi-3D numerical simulation and the experiment. Figure 11 shows the comparison of the envelopes of the crossflow displacement between the present quasi-3D numerical simulation and the experiment.

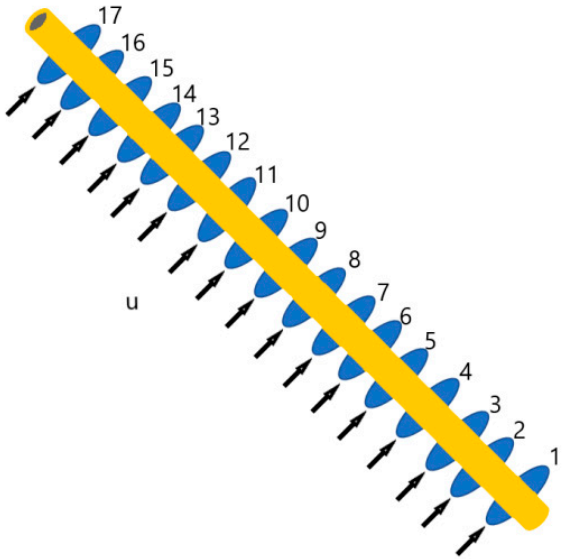

Figure 9. Slice position sketch.

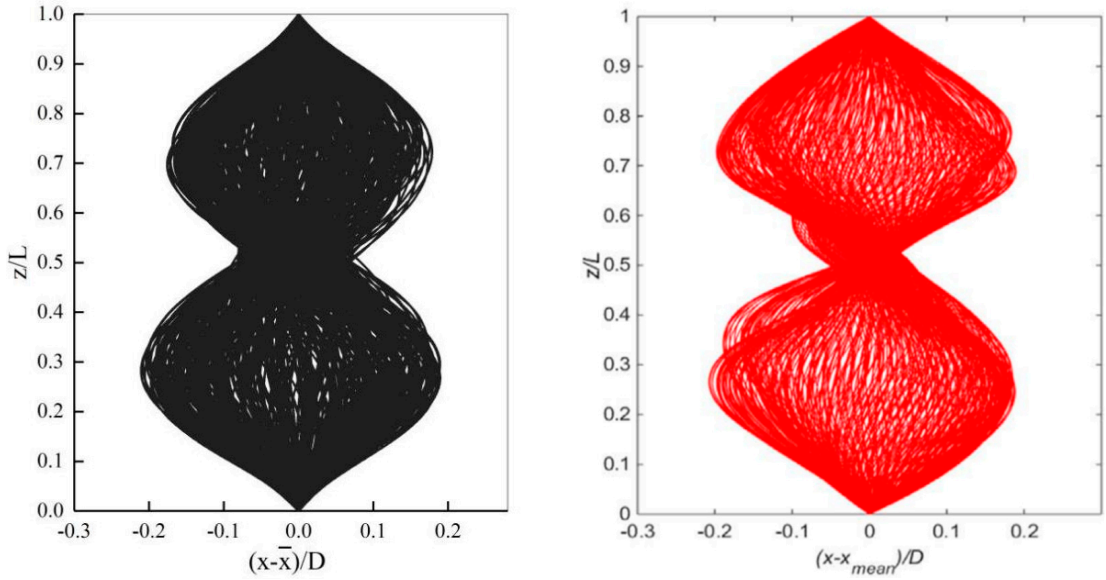

(**a**) (**b**)

Figure 10. Comparison of the riser response envelopes in IL direction. (**a**) Simulation results. (**b**) Experimental results [27].

It can be seen that the main control modes of inline and crossflow displacements obtained from the quasi-3D numerical simulation results were second-order and first-order, respectively, which is consistent with the experimental results. Although the amplitude ranges were slightly different, the envelope profile was essentially the same.

As shown in Figure 12, by comparing the displacement–time history curves in the crossflow direction of the riser at $z/L = 0.22$, it is easy to find that the amplitude range of the present quasi-3D numerical simulation is in good agreement with the original experimental results. The original experimental period was about 0.60 s, and the present CFD period was about 0.55 s, which is slightly shorter than that of the original experimental data, but the error was controlled within 8.3%. The frequency calculated from the periodic value obtained from the numerical calculation results in this paper was 1.786 Hz, which is almost the same as the first-order eigenfrequency (1.79 Hz).

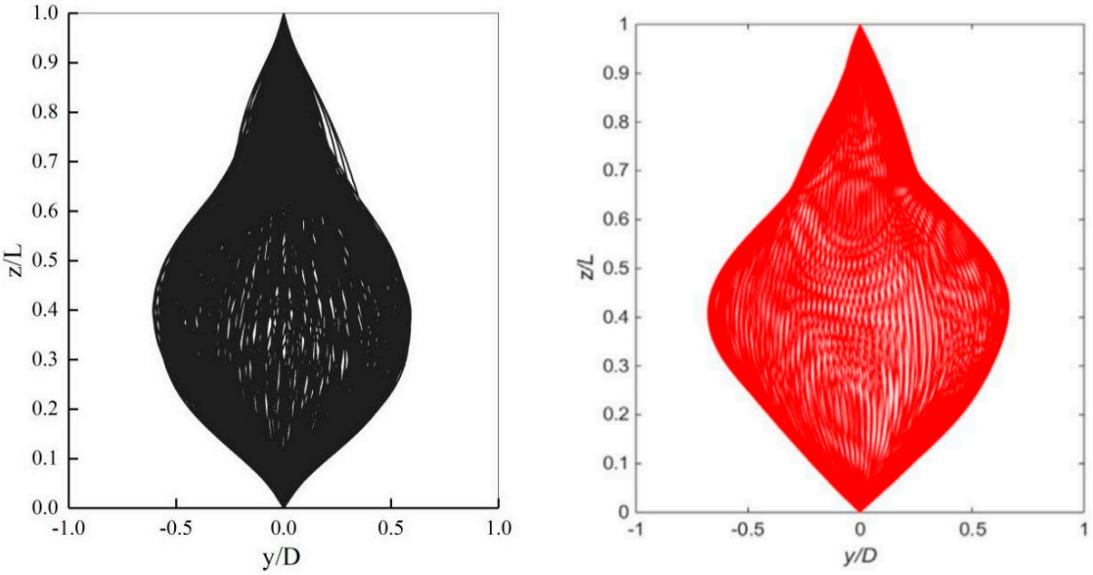

Figure 11. Comparison of the riser response envelopes in CF direction. (**a**) Simulation results. (**b**) Experimental results [31].

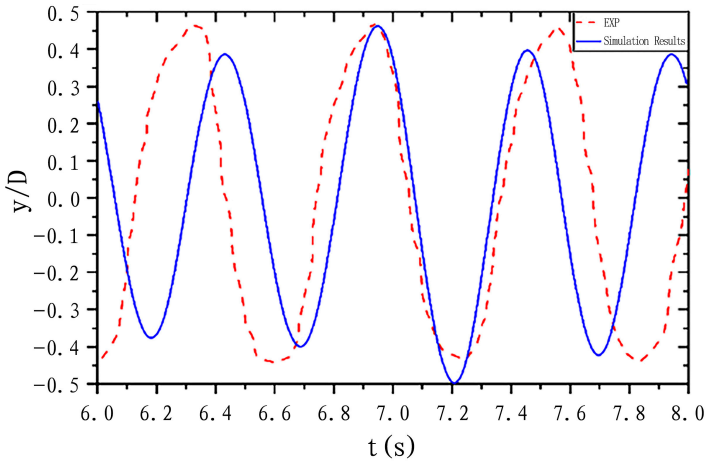

Figure 12. Displacement–time history curves in the CF direction.

According to the above analysis, the quasi-three-dimensional numerical results in this paper are in good agreement with the experimental data, indicating that the quasi-three-dimensional numerical model in this paper can accurately predict the dynamics of vortex-induced vibration.

4. Results and Discussion

4.1. Description of the Problem

Based on the quasi-3D numerical model verified above, riser models with slenderness ratios (L/D) of 400, 550 and 700 were established for numerical simulation of the VIV. The main parameters of the quasi-3D numerical model are summarized in Table 3. In this paper, simulations were performed for six different test cases, namely C1, C2, C3, C4, C5 and C6, as displayed in Table 4.

When the vortex shedding frequency of the riser approaches a certain order of natural frequency, resonance occurs, resulting in an increase in amplitude. The outer drainage basin surrounding the riser was established using the modal analysis module in ANSYS Workbench to conduct modal analysis on the riser model. Table 5 provides the first six natural frequencies of the riser in still water.

Table 3. Riser model parameters.

Parameter	Value	Unit
Diameter (D)	0.04	m
Modulus of elasticity (E)	2.74×1010	N/m^2
Top tension (T)	1500	N
Mass ratio (m *)	1.83	

*: Dimensionless.

Table 4. Six different test cases.

Case	Velocity (m/s)	Slenderness Ratios
C1	0.2	400
C2	0.2	550
C3	0.2	700
C4	0.1	700
C5	0.15	700
C6	0.25	700

Table 5. First six natural frequencies of riser model in still water.

L/D = 400	f_1(Hz)	f_2(Hz)	f_3(Hz)	f_4(Hz)	f_5(Hz)	f_6(Hz)
	0.7837	1.7136	2.6067	3.7466	5.0832	6.6353
L/D = 550	f_1(Hz)	f_2(Hz)	f_3(Hz)	f_4(Hz)	f_5(Hz)	f_6(Hz)
	0.6421	1.3103	2.0286	2.8192	3.6991	4.6824
L/D = 700	f_1(Hz)	f_2(Hz)	f_3(Hz)	f_4(Hz)	f_5(Hz)	f_6(Hz)
	0.4297	0.8695	1.3587	1.8564	2.3903	2.9675

4.2. The Displacement–Time History Curves

It can be seen from Figure 13 that the vibration amplitude variation of each node in the inline (IL) and crossflow (CF) directions gradually increased from both ends of the riser to the center of the riser. The maximum value of the average value of the IL displacement appeared at node 37 instead of node 35 at the midpoint, with an amplitude of approximately 2.081D. The maximum average value of the IL displacement was located about 2–4% below the midpoint of the riser, which was due to the gradual decrease in the top tension of each riser node along the riser axis from top to bottom.

The CF displacement reciprocated at y/D = 0, but the vibration amplitude was not stable. The vibration displacement–time history curves in the CF direction and the IL direction did not have smooth and regular sine or cosine curves similar to those in the two-dimensional VIV of a cylinder, but rather approximated the vibration trace of the two-dimensional cylinder when multi-frequency flapping occurred, which also reflects the randomness and complexity of three-dimensional VIV.

4.3. Characteristics of VIV Track of Riser

Figure 14 illustrates the mass center trajectories at 17 different slices along the riser axis.

By comparing Figure 14a–c, it can be observed that the IL and CF displacements of all slices in the riser axis increased with an increase in the slenderness ratio. As shown in Figure 14a, when L/D = 400, a clear "8"-shaped vibration trace was visible at each slice. With an increase in slenderness ratio, the "8" vibration trace of the riser became increasingly scattered from the middle position of the riser. Figure 14c demonstrates that when L/D = 700, only a faint "8"-shaped motion trace was visible at both ends of the riser.

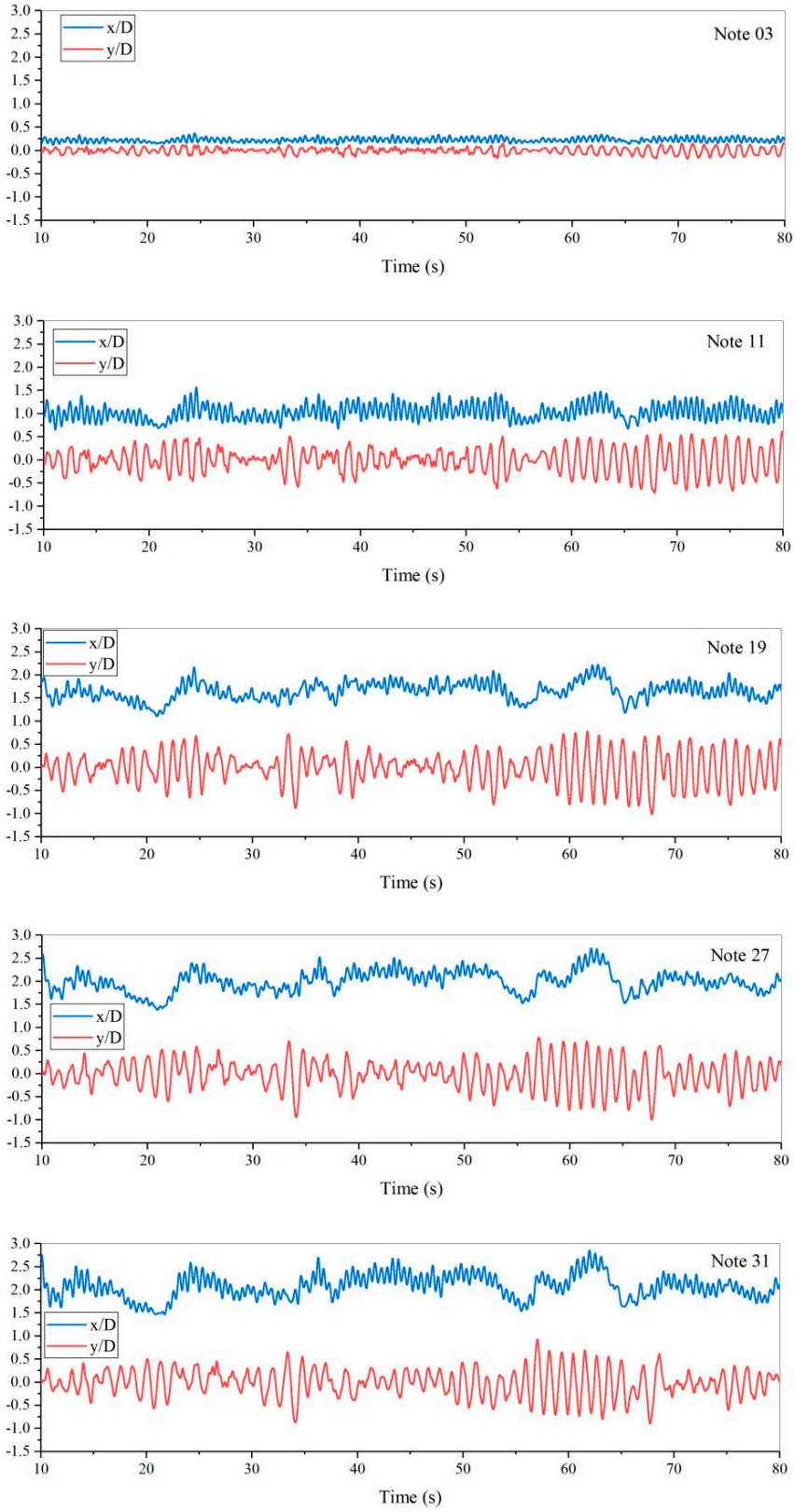

Figure 13. *Cont*.

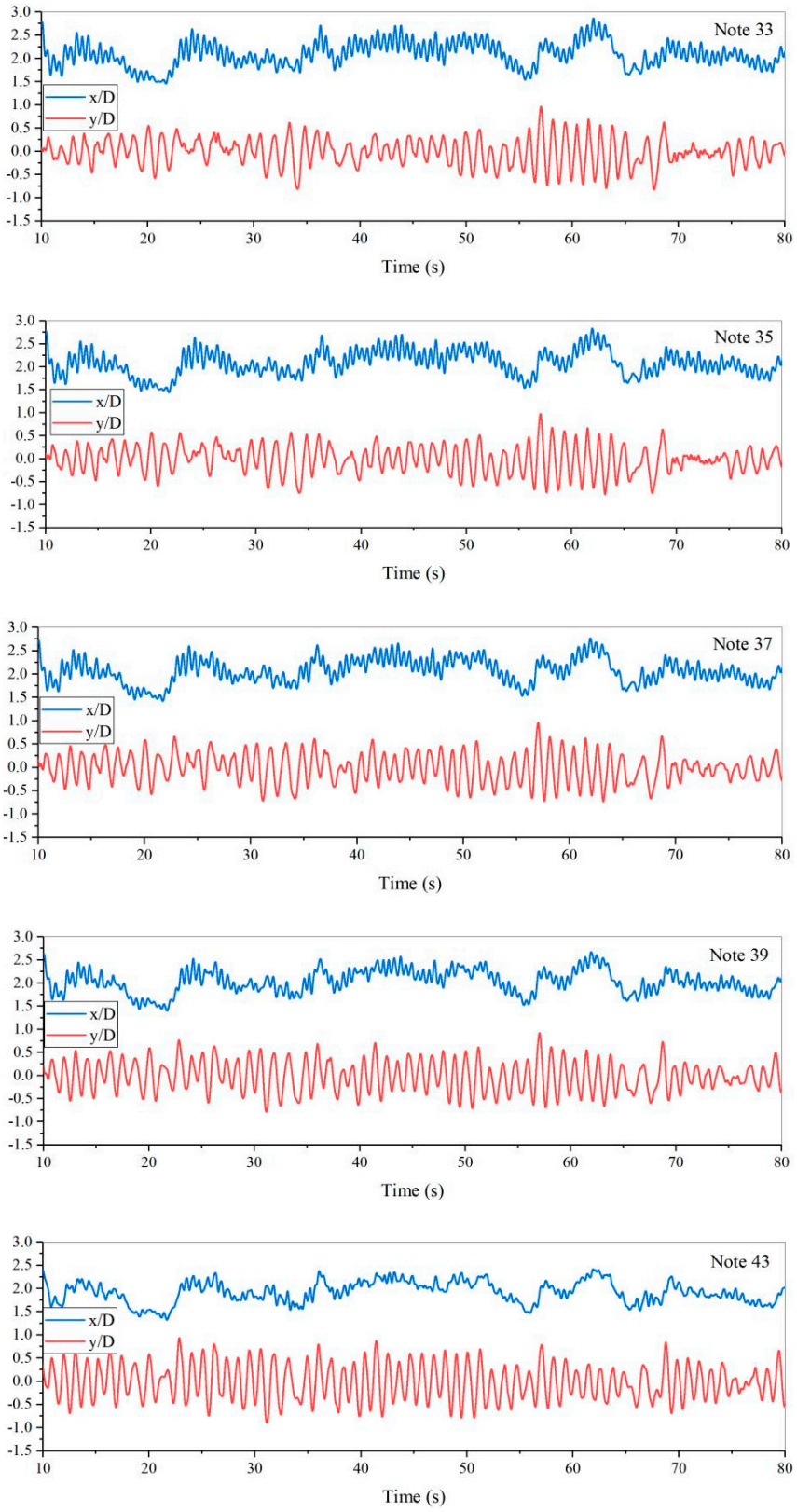

Figure 13. *Cont.*

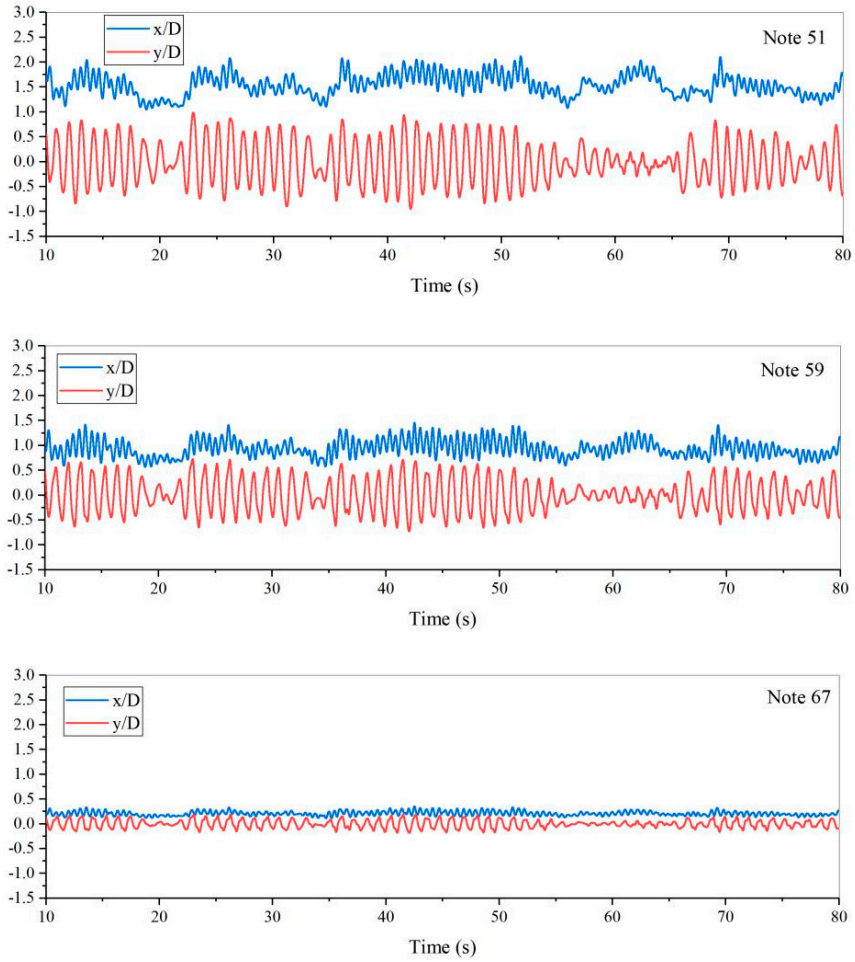

Figure 13. Displacement–time history curves of each node in the CF and IL directions.

By comparing Figure 14c–f, it can be observed that the IL and CF displacements of all slices in the riser axis increased with an increase in the flow velocity. Figure 14d reveals that a relatively "8"-shaped motion trace of the mass center could be seen for all nodes except for partial nodes in the middle section of the riser. As the flow velocity increased, the trajectory of the "8"-shaped mass center gradually became more blurred, but it remained faintly visible. When U = 0.25 m/s, as shown in Figure 14f, only a "e"k "8"-shaped motion trace was visible in the region of both ends of the riser. Furthermore, it can be observed that with an increase in flow velocity, the IL and CF displacements continuously increased at the same slenderness ratio. This is because as the flow rate increases, the fluid forces acting on the riser increase, thereby causing the equilibrium positions of the standpipe in the IL direction to increase.

The "8"-shaped vibration trace reflects the occurrence of dual resonance where the IL and CF vibration frequencies have a ratio of two [36]. Due to the influence of different slenderness ratios and flow rates, the IL and CF vibrations at different axial positions of the riser had different phase differences, leading to different figure-eight shapes on the 17 slices along the riser axis.

4.4. Vibration Modal Analysis of Riser

Figure 15 exhibits the instantaneous dimensionless displacement envelopes of the riser in the IL and CF directions, revealing that an increase in the slenderness ratio or flow velocity leads to increasingly obvious multi-modal vibration phenomenon.

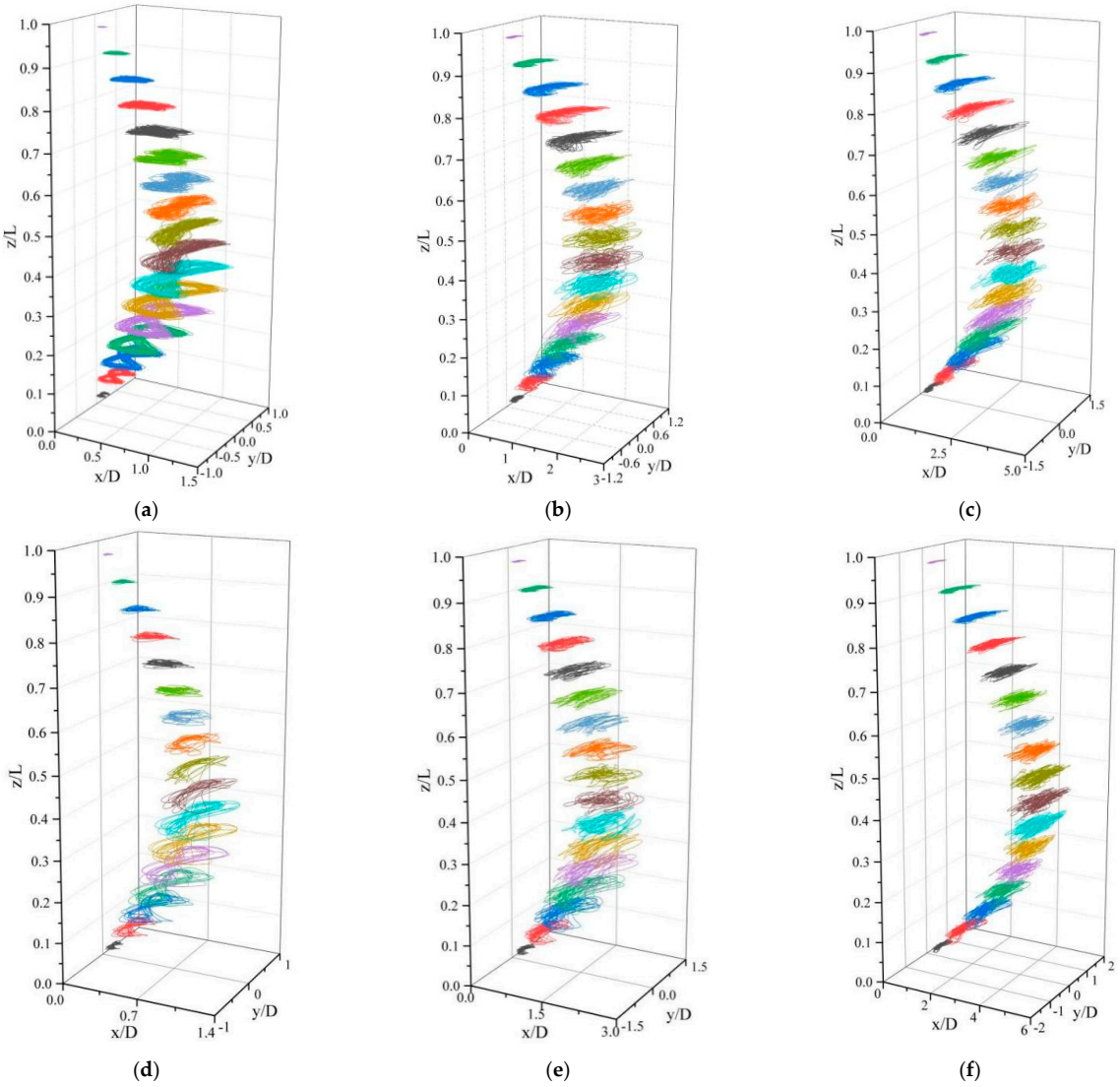

Figure 14. Trajectories of the mass centers at slices of the riser. (**a**) C1, U = 0.20 m/s, L/D = 400. (**b**) C2, U = 0.20 m/s, L/D = 550. (**c**) C3, U = 0.20 m/s, L/D = 700. (**d**) C4, U = 0.10 m/s, L/D = 700. (**e**) C5, U = 0.15 m/s, L/D = 700. (**f**) C6, U = 0.25 m/s, L/D = 700.

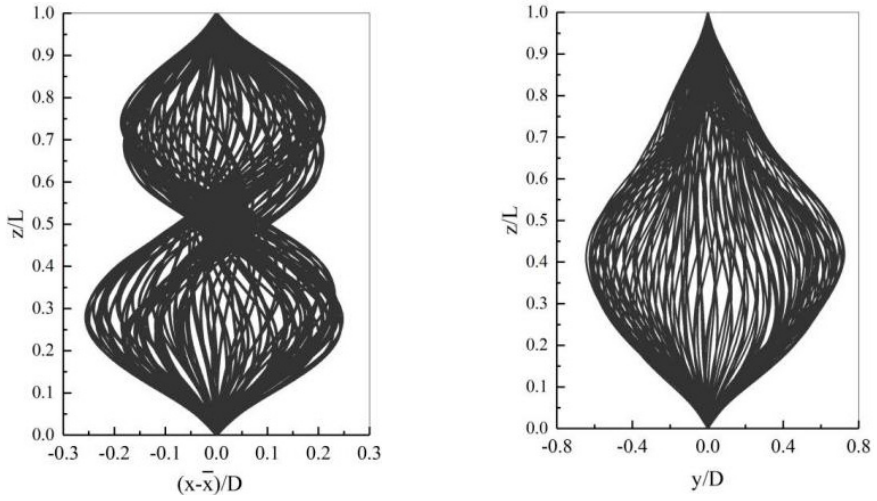

Figure 15. *Cont.*

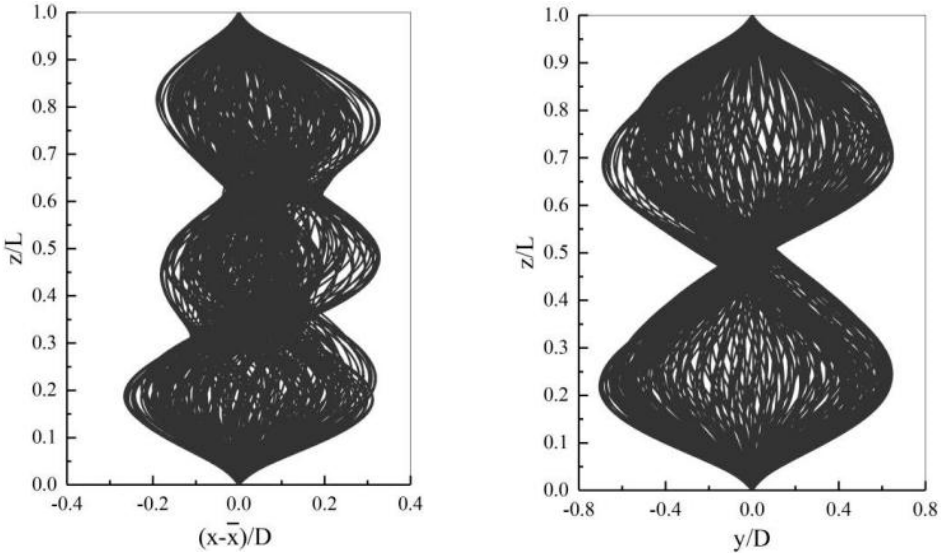

(**b**)

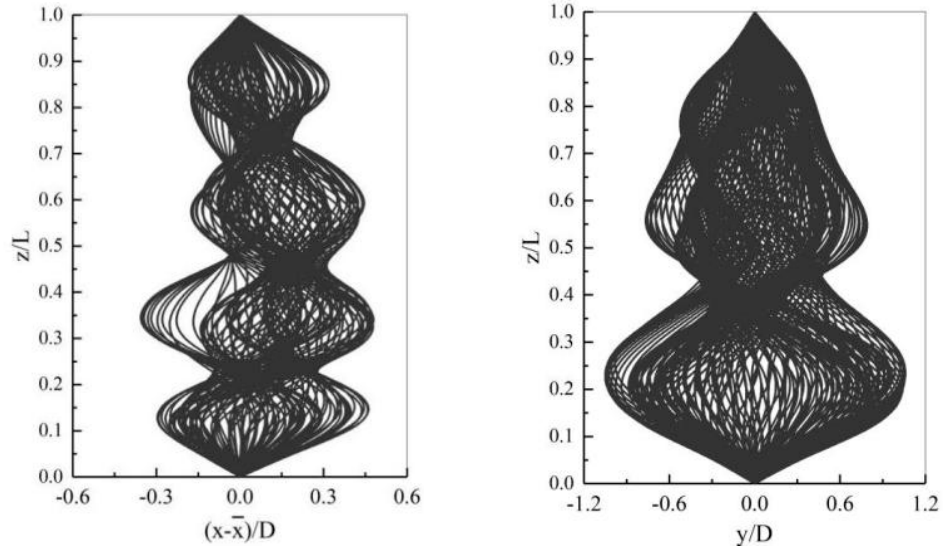

(**c**)

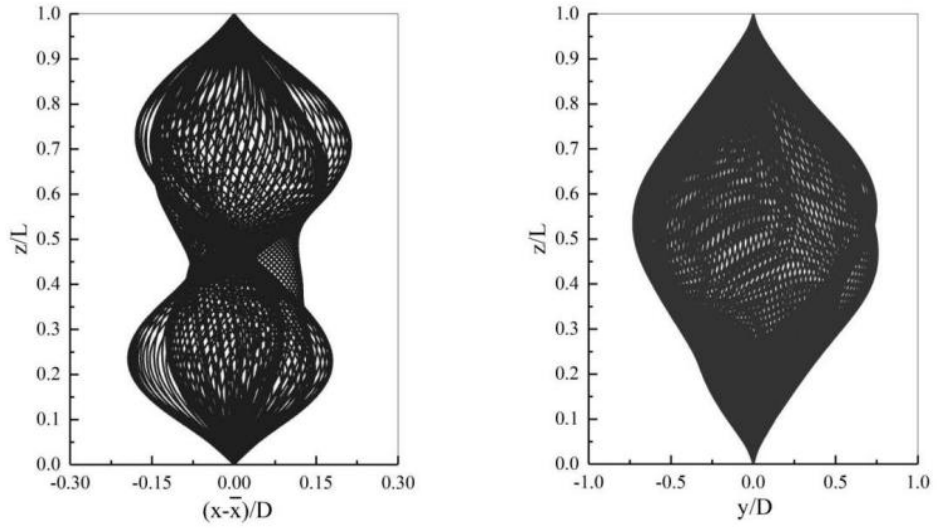

(**d**)

Figure 15. *Cont*.

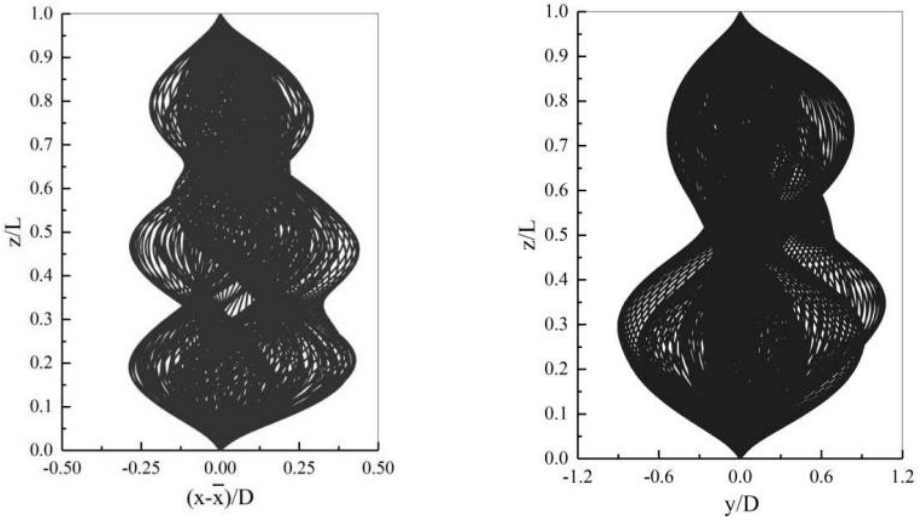

(**e**)

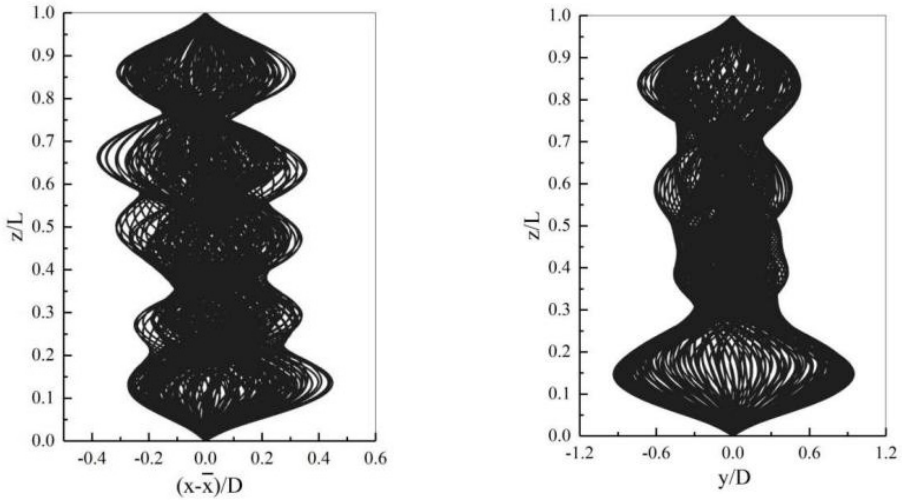

(**f**)

Figure 15. The VIV displacement envelops of the riser in the IL and CF directions. (**a**) C1, U = 0.20 m/s, L/D = 400. (**b**) C2, U = 0.20 m/s, L/D = 550. (**c**) C3, U = 0.20 m/s, L/D = 700. (**d**) C4, U = 0.10 m/s, L/D = 700. (**e**) C5, U = 0.15 m/s, L/D = 700. (**f**) C6, U = 0.25 m/s, L/D = 700.

When comparing Figure 15a–c, it was observed that an increase in the slenderness ratio resulted in a higher number of vibration modes in both the IL and CF directions. The dominant mode for the IL direction was fourth-order, while for the CF direction, it was second-order with a weak third-order mode. Such findings can be explained by two reasons: first, the Reynolds number was constant in the subcritical stage, resulting in a stable vortex shedding frequency equal to the vibration frequency when the locking phenomenon occurred; second, an increase in the slenderness ratio decreased natural frequencies while increasing the order of the natural frequencies, which resulted in more vibration modes. Moreover, due to the reduction in the difference between the natural frequencies of each order, the vibration frequency was more likely to jump to adjacent orders, leading to a further aggravation of the multi-modal vibration phenomenon.

When comparing Figure 15c–f, it was concluded that an increase in the flow velocity also resulted in an increase in the number of vibration modes in both the IL and CF directions. As the flow velocity increased, the vortex shedding frequency of the riser also increased. When the locking phenomenon occurred, the vibration frequency of each finite element node was equal to the vortex shedding frequency of the riser. Thereby, an increase in flow velocity did not affect the natural frequency of the riser but rather increased the

vibration frequency of each node, ultimately leading to a continuous increase in the number of vibration modes.

Tables 6 and 7 reveal the variation in the dominant mode with respect to the slenderness ratio and flow velocity, respectively.

Table 6. Dominant modes of the IL and CF directions at different slenderness ratios (U = 0.2 m/s).

Direction \ L/D	400	550	700
IL	2	3	4
CF	1	2	2

Table 7. Dominant modes of the IL and CF directions at different flow velocities (L/D = 700).

Direction \ U(m/s)	0.1	0.15	0.2	0.25
IL	2	3	4	5
CF	1	2	2	3

4.5. Standing and Traveling Waves

In addition, Figure 16 exhibits the displacement–time history nephogram of the vibration responses of the riser in the IL and CF directions, which reflects the changing characteristics of the riser VIV from a standing wave to a traveling wave. The dominant modes of the riser obtained from analyzing the displacement–time history nephograms are consistent with the observation results in the envelope diagrams in Figure 14. It can also be observed that as the slenderness ratio or flow velocity increased, the standing wave response gradually disappeared while the traveling wave response gradually dominated.

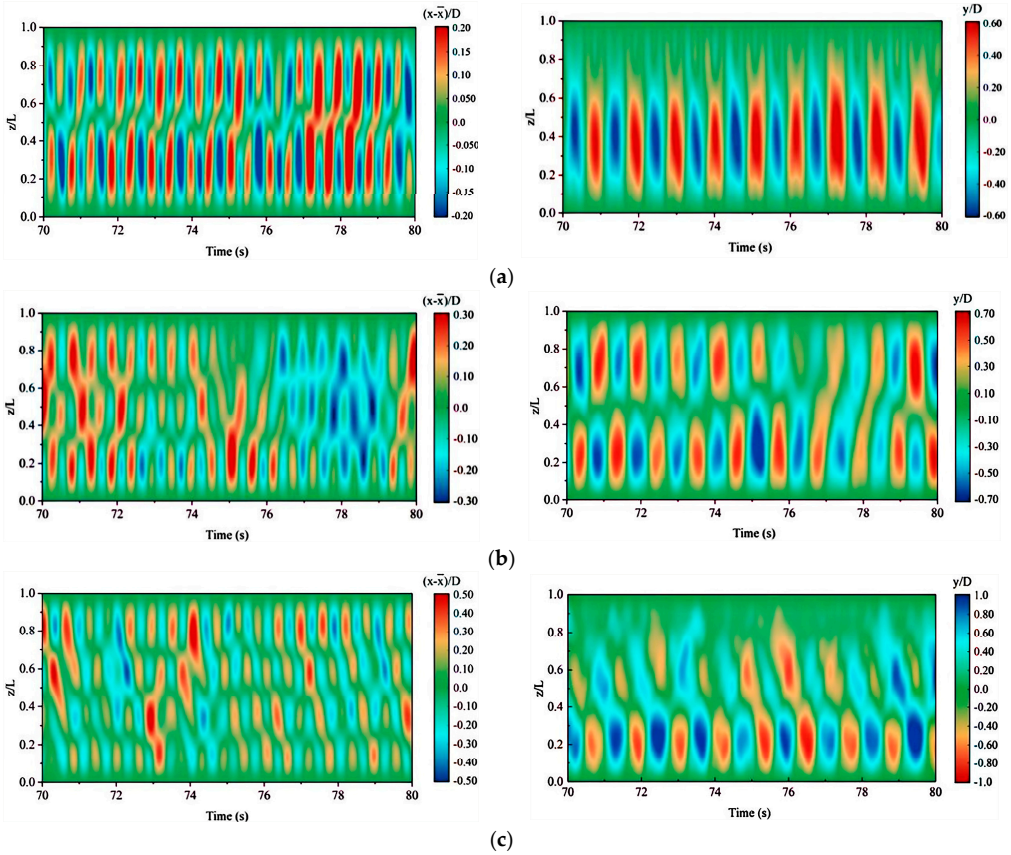

Figure 16. *Cont.*

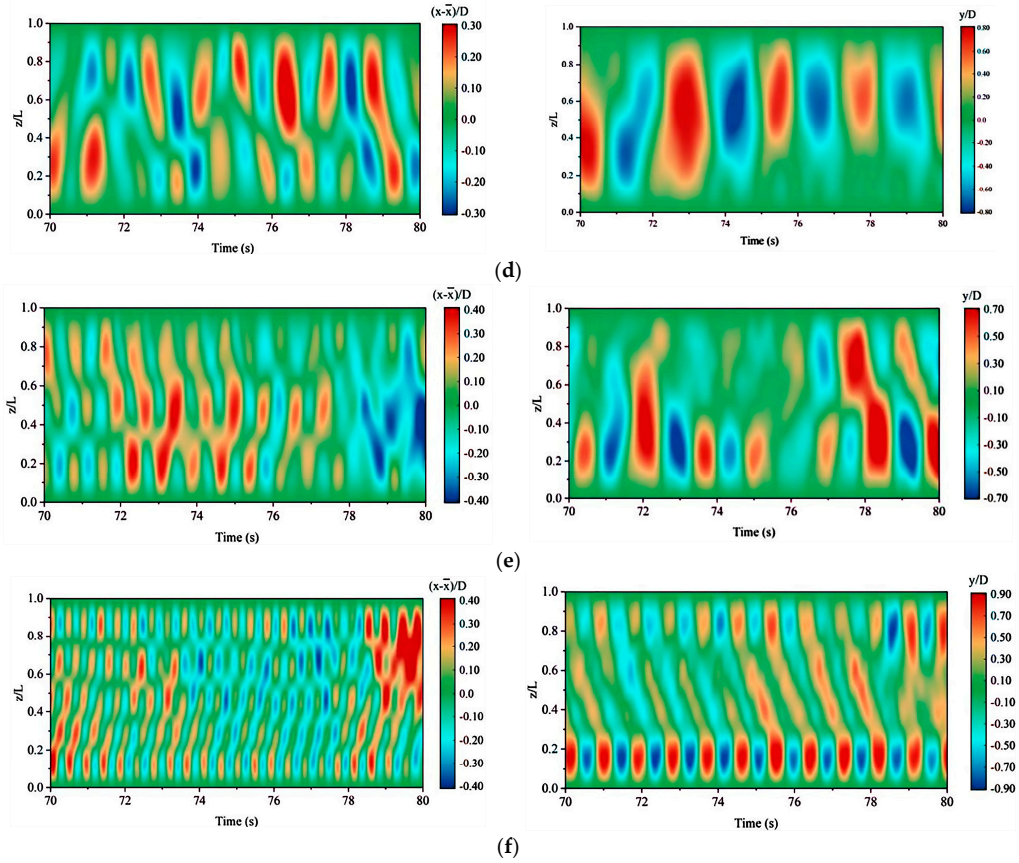

Figure 16. Time-history nephogram of riser vibration response in the IL and CF directions. (**a**) C1, U = 0.20 m/s, L/D = 400. (**b**) C2, U = 0.20 m/s, L/D = 550. (**c**) C3, U = 0.20 m/s, L/D = 700. (**d**) C4, U = 0.10 m/s, L/D = 700. (**e**) C5, U = 0.15 m/s, L/D = 700. (**f**) C6, U = 0.25 m/s, L/D = 700.

Figure 16a shows that the response of the riser in the IL direction was a weak traveling wave, while in the CF direction, it was a standing wave. Figure 16b shows the traveling wave response in the IL direction and the combination of a traveling wave and standing wave in the CF direction. Figure 16c shows significant traveling wave responses in both the IL and CF directions. This phenomenon indicates that with an increase in the slenderness ratio, the standing wave response gradually disappears, and the traveling wave response gradually dominates.

Figure 16d shows that the response of the riser in the IL direction was an unstable traveling wave, while in the CF direction, it was a standing wave. Figure 16e shows the traveling wave response in the IL direction and the combination of a traveling wave and standing wave in the CF direction. Figure 16c,f shows significant traveling wave responses in both the IL and CF directions. These phenomena lead to a conclusion consistent with the above: with an increase in the flow velocity, the traveling wave effect gradually dominates.

4.6. Riser Vibration Response Frequency Analysis

In Figure 17, the oscillation frequencies of the IL and CF directions of the riser at nine different positions along the riser axis are presented. The dominating frequency was consistent with the main mode obtained in Sections 4.4 and 4.5. The ratio of the dominating frequency of the IL vibration to the dominating frequency of the CF vibration was approximately 2.

In Figure 17a, the dominating frequency of the riser in the IL direction was 1.8456 Hz, which is close to the second-order natural frequency of 1.7136 Hz shown in Table 5. The vibration presented as the second-order main control mode with weak third-order and fourth-order frequency components. The dominating frequency of the riser in the CF direction was 0.9408 Hz, which is close to the first-order natural frequency of 0.7837 Hz, and the vibration presented as the first-order main control mode.

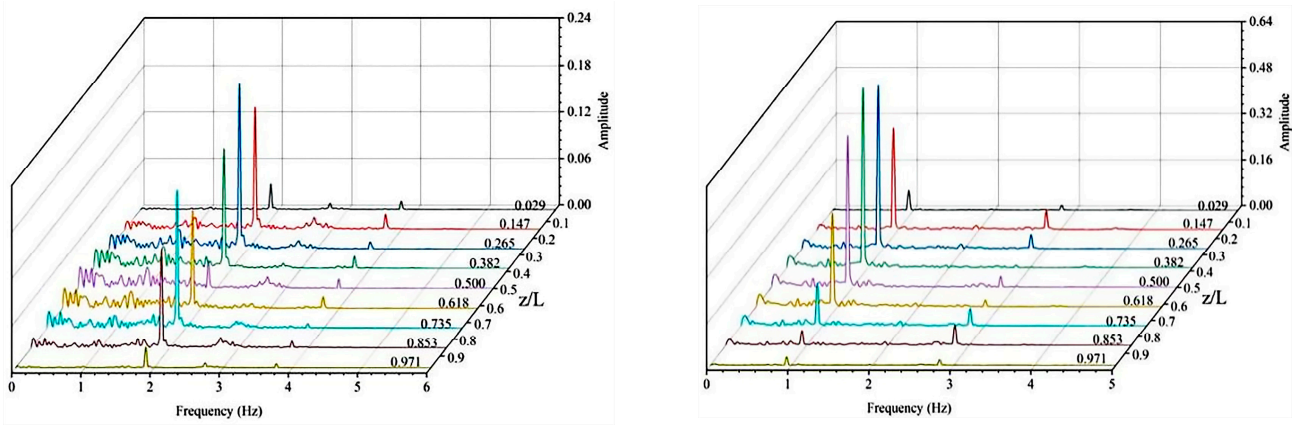

(**a**)

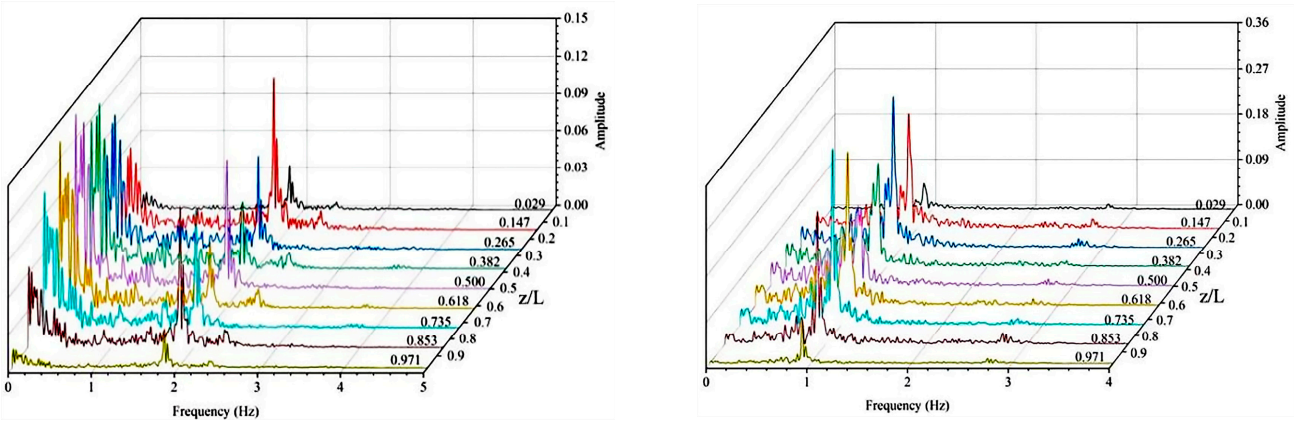

(**b**)

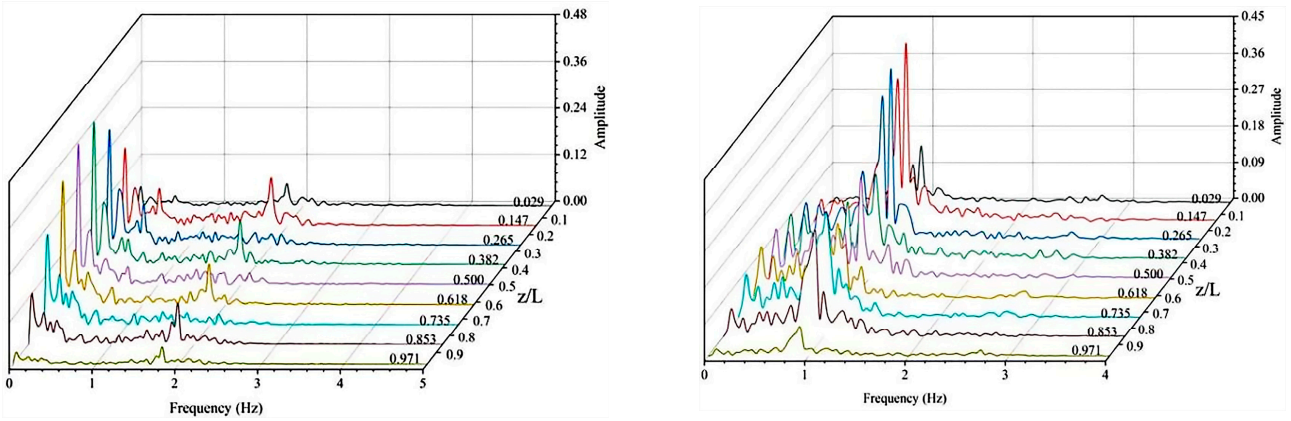

(**c**)

Figure 17. *Cont.*

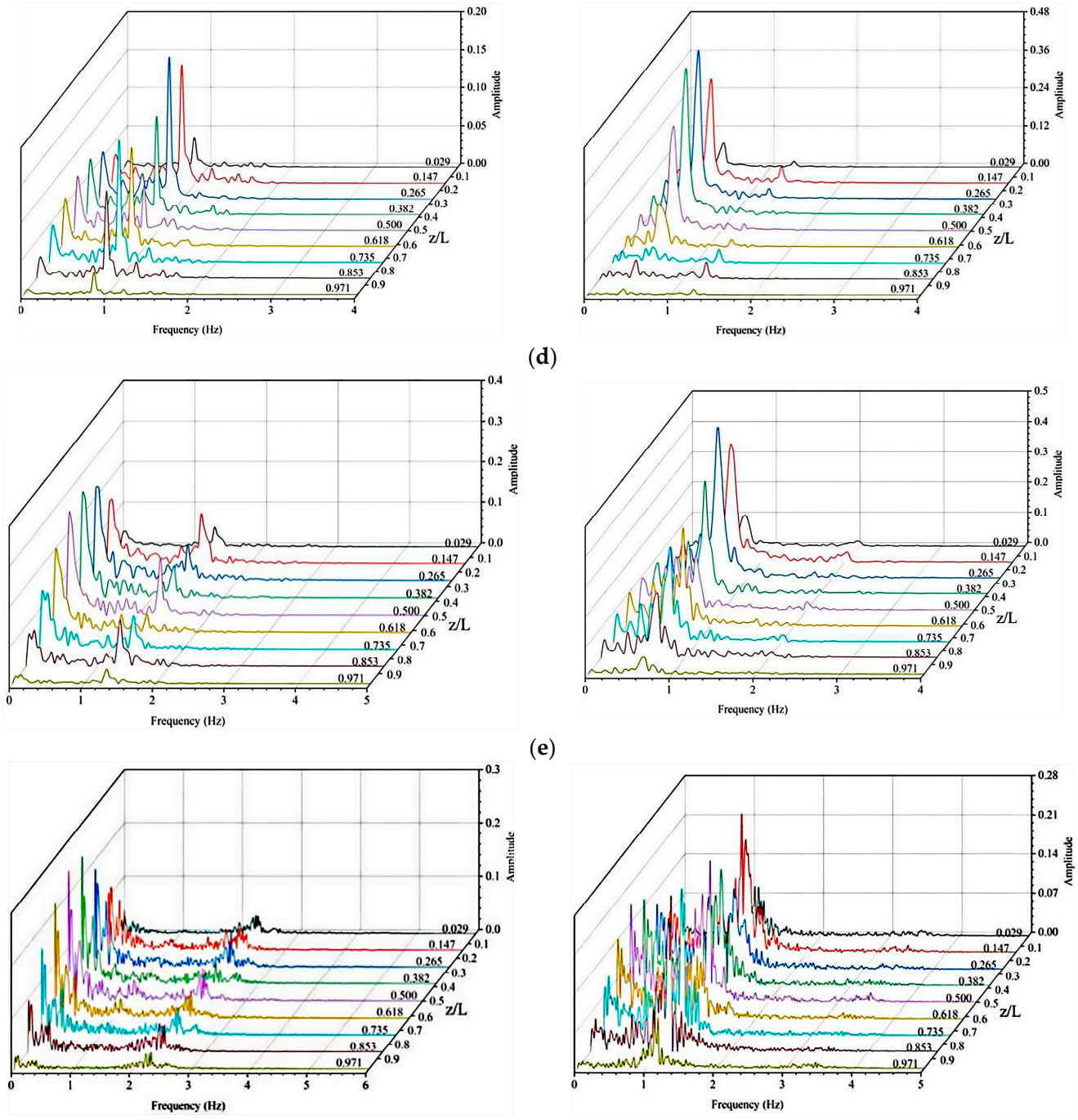

Figure 17. Frequency spectra of IL and CF vibration responses at different axial positions of the riser. (**a**) C1, U = 0.20 m/s, L/D = 400. (**b**) C2, U = 0.20 m/s, L/D = 550. (**c**) C3, U = 0.20 m/s, L/D = 700. (**d**) C4, U = 0.10 m/s, L/D = 700. (**e**) C5, U = 0.15 m/s, L/D = 700. (**f**) C6, U = 0.25 m/s, L/D = 700.

Figure 18 shows the variation in the dominating frequency of the riser in both the IL and CF directions as the slenderness ratio varied. With an increase in the slenderness ratio, the broadband characteristic of frequencies in both IL and CF directions became more prominent, leading to an aggravated degree of fatigue damage of the riser.

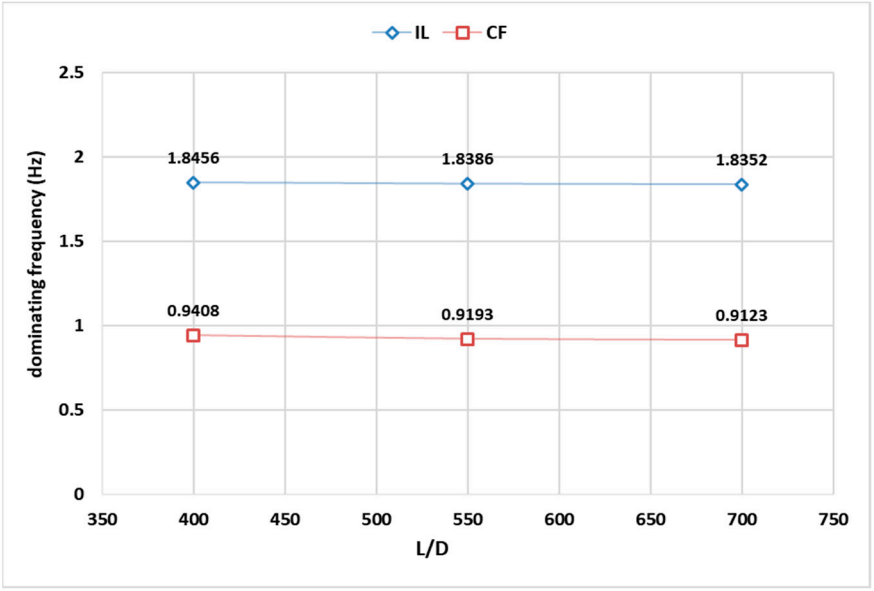

Figure 18. Dominating frequencies of IL and CF directions at different slenderness ratios (U = 0.2 m/s).

Comparative analysis of Figure 17c–f reveals that with an increase in flow velocity, the vibration frequency increased continuously, resulting in more obvious multi-frequency and wide-frequency vibration phenomena. Moreover, it can be observed from the frequency spectra in the CF direction that there were secondary frequencies which were twice or even three times the dominating frequency, representing the coupling effect of vibrations in both the IL and CF directions.

Furthermore, comparative analysis of Figure 17a–c shows that as the slenderness ratio increased, the amplitude of lower-order frequencies below the dominating frequency in the CF vibration response spectra increased continuously, which had a significant effect on the fatigue damage of the riser. This was due to the transverse average fluctuation that occurred when the transverse vibration equilibrium position of the riser deviated from y = 0, as can be vaguely seen from the transverse envelope diagram of the riser.

To conclude, Figures 17 and 19 provide valuable insights into the frequency analysis of the riser vibration response in both the IL and CF directions, demonstrating the impact of the slenderness ratio and flow velocity on the vibration frequency and characteristics of the riser.

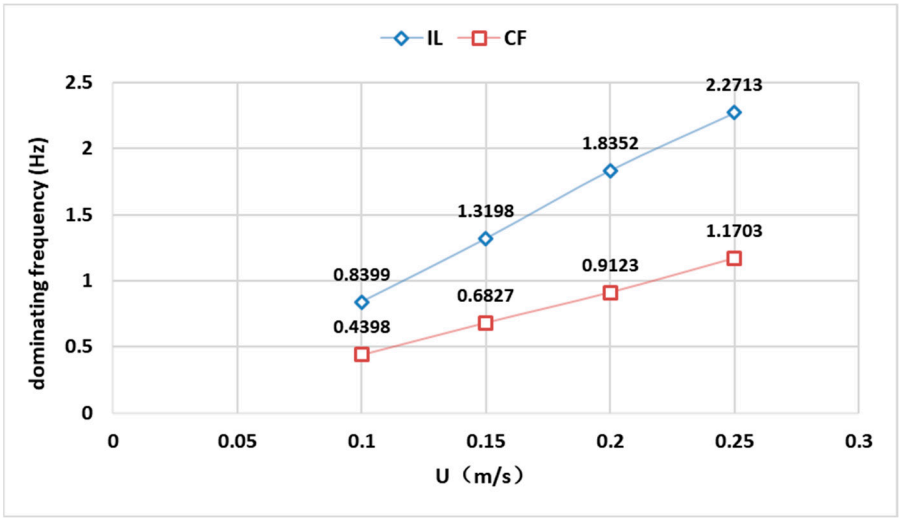

Figure 19. Dominating frequencies of IL and CF directions at different flow rates (L/D = 700).

4.7. Wake Vortex Characteristics Analysis

In Figure 20, vortex diagrams are presented for nine different positions along the riser axis (Z/L = 0.029, 0.147, 0.265, 0.382, 0.500, 0.618, 0.735, 0.853 and 0.971). The diagram clearly shows that the vortex shedding modes at various positions along the riser axis were not the same and could mainly be categorized as 2S, 2P and P + S vortex shedding modes. The 2S mode was characterized by low intensity, and the energy it carried could only support vibration with lower amplitudes. Figure 20 depicts that the 2S mode occurred primarily in areas with smaller amplitudes such as the ends of the riser and the vicinity of the vibration stagnation point. On the other hand, the vortexes in the P + S and 2P modes were more intense, and they carried enough energy to support larger amplitudes which, in turn, strengthen the vortex and maintain the P + S and 2P modes. As Figure 20 demonstrates, P + S and 2P modes tended to occur in areas with higher amplitudes in the middle of the riser.

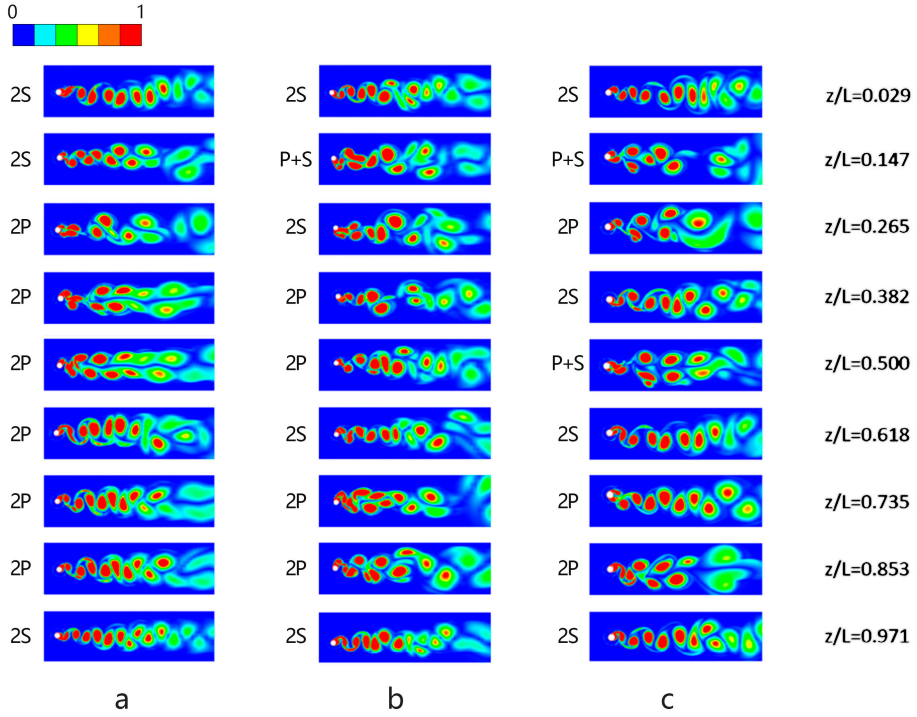

Figure 20. Vortex shedding diagram at different axial positions of riser. (**a**) C4, U = 0.10 m/s, L/D = 700. (**b**) C5, U = 0.15 m/s, L/D = 700. (**c**) C6, U = 0.25 m/s, L/D = 700.

5. Conclusions

In this paper, based on the slice method, through a self-compiled UDF program in the Fluent solver, a 3D riser structure vibration program and 2D Fluent flow field calculation were combined to achieve fluid–structure coupling, and the numerical simulation of the vortex-induced vibration of a flexible riser with different slenderness ratios and different flow velocities was carried out. The following conclusions may be drawn:

(1) Uniform flow did not result in smooth or regular sine or cosine curves for displacement–time history curves in the IL and CF directions but rather approximated to the vibration trace of a two-dimensional cylinder when multi-frequency flapping occurred. The maximum point of the riser's IL displacement balance was between 2% and 4% below the riser's midpoint;

(2) With an increase in the slenderness ratio, the equilibrium position of the vibration of the riser in the IL direction continuously increased, but the position of the maximum value of the average value of the IL displacement in the axial direction of the riser remained unchanged. The "8"-shaped vibration track of the riser became increasingly vague and chaotic while being limited to a certain range. The vibration frequencies and vibration

modes in the IL and CF directions continued to increase gradually, shifting from single-mode vibration to multi-modal vibration. At the same time, the order of the natural frequency of the vibration frequency continued to rise, and the number of vibration modes continued to increase. Furthermore, the phenomena of multi-frequency vibration and wide-frequency vibration became more apparent;

(3) With an increase in flow velocity, the equilibrium position of the vibration of the riser in the IL direction continuously increased, but the position of the maximum value of the average value of the IL displacement in the axial direction of the riser remained unchanged. The vibration frequency increased with increasing flow velocity; however, the natural frequency remained constant. Therefore, the order of the natural frequency at which the vibration frequency was located continuously increased, leading to an increase in the number of vibration modes. This phenomenon also displayed a shift from a lower-order standing wave to a higher-order traveling wave (the standing wave response gradually disappeared, and the traveling wave response gradually dominated);

(4) The 2S vortex shedding mode primarily occurred at the two ends of the riser and near the vibration stagnation point where the amplitude was relatively small. The P + S and 2P vortex shedding modes mainly occurred at places with relatively large amplitudes.

Author Contributions: Conceptualization, L.J.; methodology, L.J. and S.S.; software, F.S.; investigation, X.S.; resources, X.S.; data curation, L.J. and F.S.; writing—original draft preparation, L.J.; writing—review and editing, S.S. and L.J. All authors have read and agreed to the published version of the manuscript.

Funding: This research was funded by the NSFC and Shandong Province (U2106223); the Major Science and Technology Innovation Project in Shandong Province (2021CXGC010707); and the Natural Science Foundation of Shandong Province (ZR2022ME092).

Institutional Review Board Statement: Not applicable.

Informed Consent Statement: Not applicable.

Data Availability Statement: Not applicable.

Acknowledgments: Thanks to Wenlin Zhang to help in papers.

Conflicts of Interest: The authors declare no conflict of interest.

References

1. Gao, Y.; Zong, Z.; Zou, L.; Takagi, S. Vortex-induced vibrations and waves of a long circular cylinder predicted using a wake oscillator model. *Ocean Eng.* **2018**, *156*, 294–305. [CrossRef]
2. Vandiver, J.K. Drag Coefficients of Long Flexible Cylinders. In Proceedings of the Offshore Technology Conference, Houston, TX, USA, 2 May 1983; pp. 405–414.
3. Lie, H.; Kaasen, K.E. Modal analysis of measurements from a large-scale VIV model test of a riser in linearly sheared flow. *J. Fluids Struct.* **2006**, *22*, 557–575. [CrossRef]
4. Tognarelli, M.A.; Taggart, S.; Campbell, M. Actual VIV Fatigue Response of Full Scale Drilling Risers: With and without Suppression Devices. In Proceedings of the 27th International Conference on Offshore Mechanics and Arctic Engineering, Estoril, Portugal, 15–20 June 2008. [CrossRef]
5. Chaplin, J.R.; Bearman, P.W.; Cheng, Y.; Fontaine, E.; Graham, J.M.R.; Herfjord, K.; Huera-Huarte, F.J.; Isherwood, M.; Lambrakos, K.; Larsen, C.M.; et al. Blind predictions of laboratory measurements of vortex-induced vibrations of a tension riser. *J. Fluids Struct.* **2005**, *21*, 25–40. [CrossRef]
6. de Wilde, J.J.; Huijsmans, R.H.M. Laboratory investigation of long riser VIV response. In Proceedings of the 14th International Offshore and Polar Engineering Conference (ISOPE 2004), Toulon, France, 23–28 May 2004.
7. Tognarelli, M.A.; Slocum, S.T.; Frank, W.R.; Campbell, R.B. VIV Response of a Long Flexible Cylinder in Uniform and Linearly Sheared Currents. In Proceedings of the Offshore Technology Conference, Houston, TX, USA, 3–6 May 2004.
8. Wan, D.; Duan-Mu, Y. A Recent Review of Numerical Studies on Vortex-Induced Vibrations of Long Slender Flexible Risers in Deep Sea. *Chin. Q. Mech.* **2017**, *38*, 179–196.
9. Bishop, R.E.D.; Hassan, A.Y. The Lift and Drag Forces on a Circular Cylinder Oscillating in a Flowing Fluid. *Proc. R. Soc. Lond.* **1964**, *277*, 51–75.
10. Afra, B.; Delouei, A.A.; Tarokh, A. Flow-Induced Locomotion of a Flexible Filament in the Wake of a Cylinder in Non-Newtonian Flows. *Int. J. Mech. Sci.* **2022**, *234*, 107693. [CrossRef]

11. Facchinetti, M.L.; de Langre, E.; Biolley, F. Coupling of structure and wake oscillators in vortex-induced vibrations. *J. Fluids Struct.* **2004**, *19*, 123–140. [CrossRef]
12. Ge, F.; Long, X.; Wang, L.; Hong, Y.S. Flow-induced vibrations of long circular cylinders modeled by coupled nonlinear oscillators. *Sci. China Ser. G-Phys. Mech. Astron.* **2009**, *52*, 1086–1093. [CrossRef]
13. Li, X.M.; Guo, H.Y.; Meng, F.S. Nonlinear Coupled in-Line and Cross-Flow Vortex-Induced Vibration Analysis of Top Tensioned Riser. *China Ocean Eng.* **2010**, *24*, 749–758. [CrossRef]
14. Srinil, N. Analysis and prediction of vortex-induced vibrations of variable-tension vertical risers in linearly sheared currents. *Appl. Ocean Res.* **2011**, *33*, 41–53. [CrossRef]
15. Srinil, N.; Zanganeh, H. Modelling of coupled cross-flow/in-line vortex-induced vibrations using double Duffing and van der Pol oscillators. *Ocean Eng.* **2012**, *53*, 83–97. [CrossRef]
16. Pan, Z.Y.; Cui, W.C.; Miao, Q.M. Numerical simulation of vortex-induced vibration of a circular cylinder at low mass-damping using RANS code. *J. Fluids Struct.* **2007**, *23*, 23–37. [CrossRef]
17. Meneghini, J.R.; Saltara, F.; Fregonesi, R.D.; Yamamoto, C.T.; Casaprima, E.; Ferrari, J.A. Numerical simulations of VIV on long flexible cylinders immersed in complex flow fields. *Eur. J. Mech. B-Fluids* **2004**, *23*, 51–63. [CrossRef]
18. Afra, B.; Karimnejad, S.; Delouei, A.A.; Tarokh, A. Flow control of two tandem cylinders by a highly flexible filament: Lattice spring IB-LBM. *Ocean Eng.* **2022**, *250*, 111025. [CrossRef]
19. Schulz, K.W.; Meling, T.S. VIV analysis of a riser subjected to step and multi-directional currents. In Proceedings of the 24th International Conference on Offshore Mechanics and Arctic Engineering, Halkidiki, Greece, 12–17 June 2005.
20. Duan, M.; Wan, D.; Xue, H. Prediction of Response for Vortex-Induced Vibrations of a Flexible Riser Pipe by using Multi-Strip Method. In Proceedings of the ISOPE International Ocean and Polar Engineering Conference, Rhodes, Greece, 26 June–1 July 2016.
21. Yu, D.M.; Zou, L.; Wan, D.C. Numerical analysis of multi-modal vibrations of a vertical riser in step currents. *Ocean Eng.* **2018**, *152*, 428–442. [CrossRef]
22. Deng, D.; Fu, B.; Wan, D. Vortex-induced vibration of a flexible cylinder in an oscillatory flow. *Chin. J. Hydrodyn.* **2019**, *34*, 440–446.
23. Liu, Z.H.; Zhao, W.W.; Wan, D.C. CFD study of wave interaction with single and two tandem circular cylinders. *Ocean Eng.* **2021**, *239*, 109855. [CrossRef]
24. Han, X.X.; Lin, W.; Qiu, A.; Feng, Z.Q.; Wu, J.M.; Tang, Y.H.; Zhao, C.B. Understanding vortex-induced vibration characteristics of a long flexible marine riser by a bidirectional fluid-structure coupling method. *J. Mar. Sci. Technol.* **2020**, *25*, 620–639. [CrossRef]
25. Menter, F.R. Two-equation eddy-viscosity turbulence models for engineering applications. *AIAA J.* **1994**, *32*, 1598–1605. [CrossRef]
26. Bourguet, R.; Karniadakis, G.E.; Triantafyllou, M.S. Phasing mechanisms between the in-line and cross-flow vortex-induced vibrations of a long tensioned beam in shear flow. *Comput. Struct.* **2013**, *122*, 155–163. [CrossRef]
27. Wang, E.; Xiao, Q. Numerical simulation of vortex-induced vibration of a vertical riser in uniform and linearly sheared currents. *Ocean Eng.* **2016**, *121*, 492–515. [CrossRef]
28. Willden, R.H.J.; Graham, J.M.R. Numerical prediction of VIV on long flexible circular cylinders. *J. Fluids Struct.* **2001**, *15*, 659–669. [CrossRef]
29. Yamamoto, C.T.; Meneghini, J.R.; Saltara, F.; Fregonesi, R.A.; Ferrari, J.A. Numerical simulations of vortex-induced vibration on flexible cylinders. *J. Fluids Struct.* **2004**, *19*, 467–489. [CrossRef]
30. Clough, R.; Penzin, J.; Wang, G. *Trans. Structural Dynamics*, 2nd ed.; Higher Education Press: Beijing, China, 2007; pp. 183–185.
31. Tezdogan, T.; Demirel, Y.K.; Kellett, P.; Khorasanchi, M.; Incecik, A.; Turan, O. Full-scale unsteady RANS CFD simulations of ship behaviour and performance in head seas due to slow steaming. *Ocean Eng.* **2015**, *97*, 186–206. [CrossRef]
32. FLUENT UDFs Help Document. 2019.ANSYS. Available online: http://www.ansys.com/ (accessed on 10 September 2020).
33. Persillon, H.; Braza, M. Physical analysis of the transition to turbulence in the wake of a circular cylinder by three-dimensional Navier-Stokes simulation. *J. Fluid Mech.* **1998**, *365*, 23–88. [CrossRef]
34. Placzek, A.; Sigrist, J.F.; Hamdouni, A. Numerical simulation of an oscillating cylinder in a cross-flow at low Reynolds number: Forced and free oscillations. *Comput. Fluids* **2009**, *38*, 80–100. [CrossRef]
35. Lehn, E. *VIV Suppression Tests on High L/D Flexible Cylinders*; Norwegian Marine Technology Research Institute: Trondheim, Norway, 2003.
36. Dahl, J.M.; Hover, F.S.; Triantafyllou, M.S.; Oakley, O.H. Dual resonance in vortex-induced vibrations at subcritical and supercritical Reynolds numbers. *J. Fluid Mech.* **2010**, *643*, 395–424. [CrossRef]

Disclaimer/Publisher's Note: The statements, opinions and data contained in all publications are solely those of the individual author(s) and contributor(s) and not of MDPI and/or the editor(s). MDPI and/or the editor(s) disclaim responsibility for any injury to people or property resulting from any ideas, methods, instructions or products referred to in the content.